

1           **Long-lived (180 Myr) ductile flow within the Great Slave Lake shear zone**  
2  
3

4   **D. Šilerová<sup>1</sup>, B. Dyck<sup>2</sup>, J. A. Cutts<sup>2,3</sup>, and K. Larson<sup>2</sup>**

5   <sup>1</sup>Department of Earth Sciences, Simon Fraser University, Burnaby, BC, Canada

6   <sup>2</sup>Department of Earth, Environmental and Geographical Sciences, University of British  
7   Columbia, Kelowna, BC, Canada

8   <sup>3</sup>Geological Survey of Canada, 601 Booth Street, K1A 0E8, Ottawa, ON, Canada  
9

10   Corresponding author: Dana Šilerová (dana.silerova@smu.ca)  
11

12   **Key Points:**

- 13       • (Re)crystallized apatite and titanite record a near-continuous history of ductile shear  
14       spanning ca. 1920–1740 Ma.
- 15       • Strain was initially (ca. 1920–1880 Ma) accommodated by two coeval fault strands.
- 16       • A faultward younging in the timing of (re)crystallization is consistent with strain  
17       localization during cooling and exhumation.

## 18 Abstract

19 The Great Slave Lake shear zone (GSLsz) is a type example for deeply eroded continental  
20 transform boundaries located in the Northwest Territories, Canada. Formed during the oblique  
21 convergence of the Archean Rae and Slave cratons, the GSLsz has accommodated up to 700 km  
22 of dextral shear. Here we present the results of *in situ* U-Pb apatite and titanite geochronology  
23 from 11 samples that were collected across the strike of the shear zone. Both geochronometers  
24 record a near-continuous history of ductile shear during crustal cooling and exhumation that  
25 spans ca. 1920–1740 Ma. By integrating the geochronological data with structural and  
26 metamorphic observations across the structure, we propose a tectonic model for the shear zone  
27 that consists of three stages. The first stage (ca. 1920–1880 Ma) is characterized by strain  
28 accommodation along two coeval fault strands. During the second stage (ca. 1880–1800 Ma),  
29 ductile shear ceases along the northernmost fault strand and the locus of strain migrates  
30 southwards towards the hinterland of the Rae cratonic margin. In the third stage (ca. 1800–1740  
31 Ma), ductile strain localizes back along the southern of the two original fault strands, after which  
32 the present-day surface level of the shear zone transitions to brittle shear. Our results highlight  
33 both the significance of the lateral migration of the zone of active deformation in major crustal  
34 shear zones as well as the localization of strain along existing crustal structures.

## 35 1 Introduction

36 Crustal-scale shear zones preserve a record of the temporal and structural evolution of the  
37 ductile portions of continental plate boundaries. Over the past few decades, there has been  
38 extensive research into the rheological behavior of crustal-scale shear zones (e.g., Scholz, 1988;  
39 Sibson, 1977, 1983) leading to a robust understanding of the physical manifestation of plate  
40 boundaries at depth (Cawood & Platt, 2021; Lusk & Platt, 2020; Platt & Behr, 2011). However,  
41 despite the integral role of these structures in controlling lithospheric strength over long  
42 geological periods, there is a general lack of data related to the spatial and temporal evolution of  
43 crustal-scale shear zones. The challenges associated with collecting and interpreting  
44 geochronological data in shear zones reflect the inherent complexity of shear zone histories as  
45 well as the effects of various processes on isotopic diffusion in mineral systems (see Oriolo et al.,  
46 2018 and references therein).

47 The Paleoproterozoic Great Slave Lake shear zone (GSLsz), located in the Northwest  
48 Territories, Canada, is a crustal-scale dextral transcurrent structure that marks the boundary  
49 between the Archean Rae and Slave cratons (Hanmer, 1988; Hanmer & Lucas, 1985; Hoffman,  
50 1987). Stretching over 1000 km in length, and reaching up to 25 km in width, the GSLsz is one  
51 of the largest and best exposed Paleoproterozoic continental transform boundaries in the world.  
52 The GSLsz formed as a result of oblique convergence between those cratons, following initial  
53 collision ca. 1.95 Ga (Cutts & Dyck, 2022; Gibb & Thomas, 1977).

54 Extensive surface erosion synchronous with deformation along the GSLsz resulted in the  
55 exposure of a series of distinct mylonitic belts within the shear zone (Hanmer, 1988; Hanmer &  
56 Lucas, 1985) that preserve a continuous range of metamorphic conditions from the lower  
57 greenschist to granulite facies (Hanmer & Lucas, 1985). These mylonitic belts effectively  
58 comprise metamorphic units that exhibit decreasing width with decreasing metamorphic grade;  
59 the narrower, greenschist-grade belts are overprinted by brittle deformation features (Dyck et al.,  
60 2021; Hanmer, 1988; Hanmer et al., 1992). Because these observations are consistent with  
61 previously published fault zone models (e.g., Scholz, 1988; Sibson, 1977, 1983), the GSLsz has

62 long been identified as a type example for deeply eroded continental transform boundaries (Dyck  
63 et al., 2021; Hanmer, 1988).

64 Although recent work has answered some of the fundamental questions surrounding the  
65 structure and metamorphic evolution of the GSLsz (Cutts & Dyck, 2022; Dyck et al., 2021), the  
66 timing of shear along the plate boundary remains poorly quantified. In this study, we document  
67 the timing of (re)crystallization of apatite and titanite along the GSLsz and integrate the results  
68 with petrographic and geochemical observations. In doing so, the dates are interpreted as  
69 reflecting shear-induced (re)crystallization and, thus, provide constraint on the duration of  
70 ductile shear in the GSLsz. We present a tectonic model for the GSLsz that can serve as a  
71 framework for elucidating histories of other transcurrent continental shear zones, both modern  
72 and extinct. This work highlights the importance of integrating various sources of data in order to  
73 overcome the challenges associated with interpreting geochronological data in geologically  
74 complex systems.

## 75 **2 Geological context**

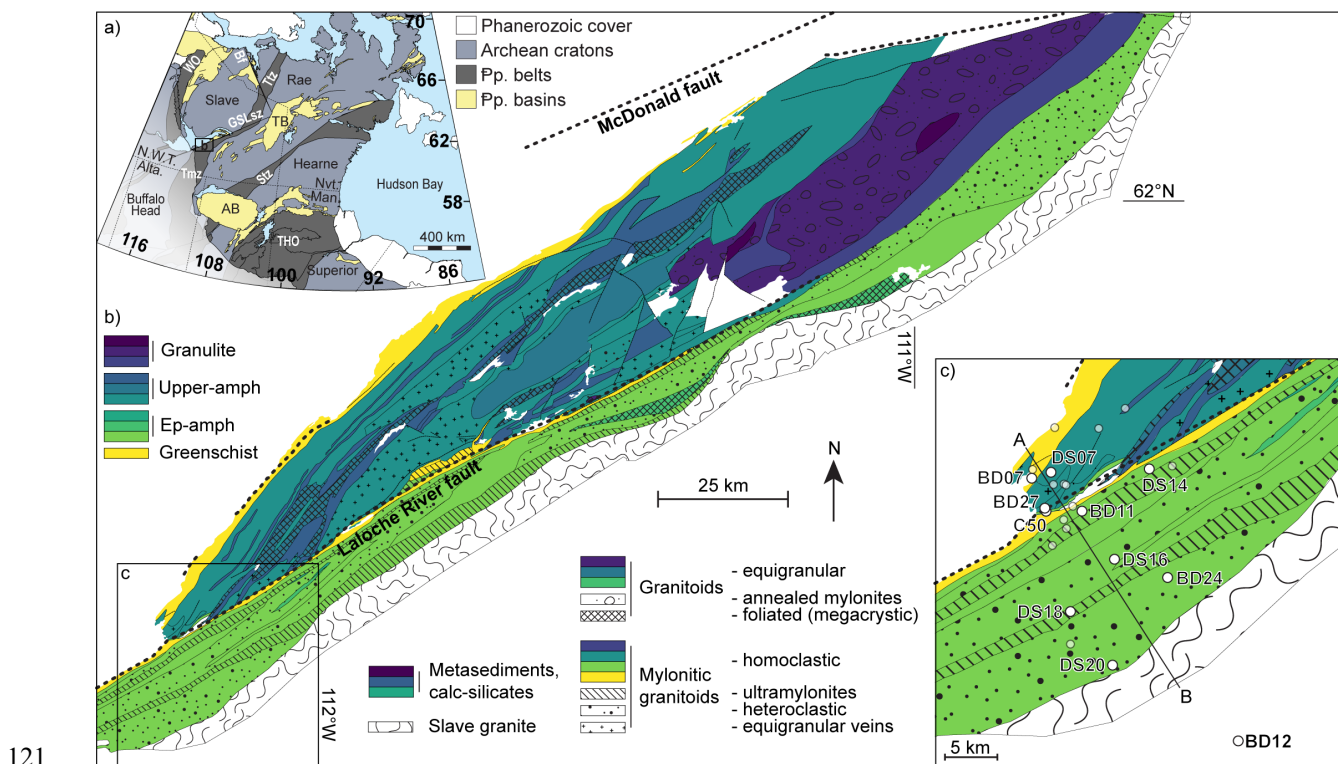
76 Northwestern Laurentia is an amalgamation of the Archean Slave, Rae, Hearne, and  
77 Superior cratons that were assembled along a series of distinct Paleoproterozoic orogenic belts.  
78 From west to east these belts include the Wopmay Orogen, the Taltson magmatic zone, the  
79 Thelon tectonic zone, the Snowbird tectonic zone, and the Trans-Hudson Orogen (Fig. 1a;  
80 Hoffman, 1988). The western boundary of the Rae craton is itself divided into three segments,  
81 with the GSLsz forming the central segment. To the northeast of the GSLsz, the Thelon tectonic  
82 zone marks the boundary between the Slave and Rae cratons, and to the southwest, the Taltson  
83 magmatic zone separates the Rae craton from the Kiskatinaw-Chinchaga-Buffalo Head  
84 Superterrane.

85 The combined Taltson-Thelon margin was initially thought to have formed due to the  
86 subduction of oceanic crust beneath the Rae craton and the ensuing collision between Slave and  
87 Rae ca. 1.97 Ga (Hoffman, 1987; Thériault, 1992). Recent geochemical and geochronologic  
88 work, however, has led to the recognition of the Taltson magmatic zone and Thelon tectonic  
89 zone as two distinct structures, rather than one contiguous margin that was dextrally offset by the  
90 GSLsz (Berman et al., 2018; Card et al., 2014). The Thelon tectonic zone records older  
91 magmatic ages (2.07–1.92 Ga; Berman et al., 2018) and younger metamorphic ages (1.92–1.89  
92 Ga; Berman et al., 2018) than the Taltson magmatic zone, which records younger magmatic ages  
93 (1.99–1.92 Ga; Bostock et al., 1987, 1991; Bostock & Loveridge, 1988; Chacko et al., 2000) and  
94 older metamorphic ages (1.94–1.92 Ga; Bethune et al., 2013; McDonough et al., 2011).

95 The GSLsz extends over 1000 km, from the foothills of the Rocky Mountains in the west  
96 to the Thelon Basin in the east (Fig. 1a). With the western half of the structure covered by  
97 Phanerozoic sedimentary rocks, exposure of the ductile structures is restricted to its eastern half  
98 where recent glaciation has contributed to near-continuous exposure of northeast striking  
99 mylonite belts. Two major brittle faults run parallel to the strike of the mylonite foliation; the  
100 McDonald fault and the Laloche River fault (Fig. 1b). The McDonald fault marks the northern  
101 boundary of the GSLsz, separating ultramylonites from the moderately deformed plutonic rocks  
102 of the Slave craton (Cutts et al., 2022), while the Laloche River fault bisects the center of the  
103 shear zone.

104 This study focuses on the westernmost segment of the exposed GSLsz (Fig. 1c) where the  
 105 Laloche River fault separates two distinct structural domains. South of the Laloche River fault,  
 106 the mylonitic foliation strikes NE–SW, parallel to the strike of the fault, and preserves epidote-  
 107 amphibolite to greenschist facies metamorphic assemblages. To the north, the foliation strikes  
 108 NNE-SSW and is truncated by the Laloche River fault. This northern structural domain preserves  
 109 a series of parallel mylonite belts that last equilibrated under a wide range of metamorphic facies  
 110 from granulite through to greenschist. The boundaries between metamorphic units are diffuse  
 111 with higher-grade units overprinted by lower-grade mineral assemblages (Dyck et al., 2021).  
 112 Accordingly, we define the boundaries between units by the appearance of the lower-grade  
 113 mineral assemblage (retrograde index minerals).

114 Rocks from the granulite, upper-amphibolite and epidote-amphibolite belts all reached  
 115 similar peak metamorphic conditions ( $\sim 0.85$  GPa,  $\sim 750$  °C), while the final stages of equilibrium  
 116 recorded by all samples collectively define a single metamorphic field gradient of  $\sim 1,000$   
 117 °C/GPa across the shear zone (Dyck et al., 2021). These findings are consistent with the  
 118 interpretation of Dyck et al. (2021) that the various mylonitic belts of the GSLsz developed over  
 119 the course of a single progressive deformation event rather than during temporally distinct  
 120 events.



121  
 122 **Figure 1.** (a) Simplified bedrock map of northern Laurentia showing the positions of Archean  
 123 cratons and other major tectonic elements, including the Great Slave Lake shear zone (GSLsz),  
 124 Bathurst fault (Bf), Taltson magmatic zone (Tmz), Thelon tectonic zone (Ttz), Snowbird tectonic  
 125 zone (Stz), Wopmay Orogen (WO), Trans-Hudson Orogen (THO), Thelon Basin (TB), and  
 126 Athabasca Basin (AB). N.W.T – Northwest Territories, Alta. – Alberta, Nvt. – Nunavut, Man. –  
 127 Manitoba. (b) Metamorphic units of the southwestern segment of the GSLsz. Units are based on  
 128 protolith lithology as mapped by Hanmer (1988). (c) Field area with sample locations

129 (translucent white circles) and transect line; location shown in 1b. Samples used for accessory  
130 mineral petrochronology are labeled and marked by larger opaque white circles.

### 131 2.1 Previous geochronological work

132 Although several decades have passed since the GSLsz was first recognized as a major  
133 tectonic structure in northwestern Laurentia, there is a lack of modern geochronologic  
134 information for the timing and duration of ductile shear. Early attempts to date the structure used  
135 U-Pb ID-TIMS geochronology on zircon and the results were interpreted to indicate that peak  
136 activity of the shear zone occurred at ca. 1.980–1.924 Ga along its southwestern segment  
137 (Hanmer et al., 1992) and by  $1978 \pm 5$  Ma along its northeastern segment (van Breemen et al.,  
138 1990). Transform motion along the shear zone was proposed to be bracketed between ca. 2.00–  
139 1.86 Ga (Bowring et al., 1984; Hanmer et al., 1992). However, the dates used to inform the  
140 timing of transform movement relied on geochronology from the host mylonitic granitoids or on  
141 interpretations of cross-cutting relationships between intrusive units and the mylonites rather  
142 than directly dating shear-induced recrystallization. Following its main period of activity, the  
143 GSLsz was offset dextrally by the McDonald fault. Late synkinematic dyke emplacement and  
144 biotite cooling ages constrain the onset of brittle deformation along the McDonald fault and  
145 conjugate Bathurst fault to ca. 1840 Ma, while a depositional age of ca. 1758 Ma for nearby  
146 synorogenic basin units has been proposed to bracket the end of brittle activity in the McDonald-  
147 Bathurst fault system (Ma et al., 2020; Rainbird & Davis, 2007).

148 Recent geochronological work done on samples from the southwestern segment of the  
149 GSLsz found that zircon and monazite U-Pb ages are unrelated to the transcurrent motion of the  
150 shear zone and, instead, record a margin-wide crustal thickening event associated with  
151 convergence of the Slave and Rae cratons (Cutts & Dyck, 2022). The timing of the peak  
152 metamorphism associated with crustal thickening is best informed by two garnet Lu-Hf ages of  
153  $1931 \pm 12$  and  $1917 \pm 6$  Ma, which overlap the ca. 1933–1913 Ma age range recorded by zircon  
154 and monazite (Cutts & Dyck, 2022). Based on the observations of suprasolidus shear  
155 microstructures (Dyck et al., 2021; Hanmer et al., 1992), the maximum age of ductile shear along  
156 the GSLsz has been interpreted to coincide with the final stages of peak metamorphism at ca.  
157 1920–1910 Ma (Cutts & Dyck, 2022).

## 158 3 Methods

### 159 3.1 Apatite and titanite geochronology

160 We conducted a ~15 km across-strike transect through the GSLsz to evaluate the record  
161 of shear-induced (re)crystallization preserved therein. Along the transect, we recorded the  
162 orientation of ductile fabrics as well as the characteristic metamorphic mineral assemblages. We  
163 collected 22 samples from which 11 were selected for *in-situ* U-Th-Pb accessory mineral  
164 petrochronology (Fig. 1c). Given the apparent lack of sensitivity of zircon and monazite to  
165 record the timing of deformation (Cutts & Dyck, 2022), we focused our study on apatite and  
166 titanite. Both minerals have a well-documented tendency to recrystallize during ductile  
167 deformation (e.g., Gordon et al., 2021; Kavanagh-Lepage et al., 2022; Moser et al., 2022; Odlum  
168 & Stockli, 2020; Ribeiro et al., 2020; Walters et al., 2022). Ten of the eleven samples are apatite-  
169 bearing and ten are titanite-bearing.

170 Target apatite and titanite grains were first identified in thin section using transmitted  
171 light microscopy. Following this, we collected backscattered electron (BSE; apatite, titanite) and  
172 cathodoluminescence (CL; apatite) images to determine the relationship of each grain with  
173 ductile fabrics and to identify zoning within individual grains. BSE imaging was done using the  
174 Tescan Mira 3 XMU field emission scanning electron microscope (SEM) at the Fipke  
175 Laboratory for Trace Element Research (FiLTER) at the University of British Columbia,  
176 Okanagan. For CL imaging, we used a Thermo Prisma tungsten-source SEM equipped with a  
177 four-channel polychromatic CL camera housed in the Department of Earth Sciences at Simon  
178 Fraser University. For both BSE and CL, we coated the samples with ~10 nm of carbon and used  
179 an accelerated voltage of 15 kV at a working distance of 10 mm.

180 *In-situ* U-Pb isotope and trace element analyses of apatite and titanite was carried out via  
181 laser ablation inductively coupled plasma mass spectrometry (LA-ICP-MS) in the FiLTER  
182 facility at the University of British Columbia, Okanagan. In total, twelve separate analytical  
183 sessions were run (four with apatite; eight with titanite). All spot analyses within individual  
184 samples were collected during the same session, except the titanite in GSL-18-C50, for which  
185 data were collected across two sessions. Five of the titanite sessions used a Photon Machines  
186 Analyte 193nm ArF excimer laser ablation system coupled to an Agilent 8900 Triple Quadrupole  
187 (QQQ) ICP-MS operated in single-quad mode. The other three titanite sessions and all four  
188 apatite sessions used an ESI New Wave Research 193nm ArF excimer laser ablation system  
189 coupled to an Agilent 8900 QQQ-ICP-MS operated in single-quad mode. Each session consisted  
190 of analyses of one to three apatite- or titanite-bearing samples. U-Pb isotopic ratios and trace  
191 element concentrations were collected from the same ablated spot volumes. Instrumentation  
192 settings for each analytical session are provided in Table S1. All U-Pb isotope and trace element  
193 data collected for unknowns and reference materials are presented in Tables S2 and S3 for  
194 apatite and titanite, respectively.

195 Apatite grains were ablated using a fluence of 4.00 J/cm<sup>2</sup>, an ablation frequency of 8.00  
196 Hz, and a spot size of 40 μm. Titanite grains were ablated using a fluence of 4.00–4.95 J/cm<sup>2</sup>, an  
197 ablation frequency of 8.00 Hz, and a spot size between 25–40 μm. Prior to each spot analysis,  
198 the surface was pre-ablated with two laser pulses to clear the sample surface of debris. The  
199 acquisition run for each spot analysis lasted between 25–30 seconds and was followed by a  
200 washout period, lasting 10 seconds. Blocks of 8–10 unknown analyses were separated by  
201 analyses of reference materials for calibration purposes and to correct for instrumental drift and  
202 down-hole fractionation.

203 The primary reference material used for all apatite U-Pb LA-ICP-MS analyses was  
204 MAD1 (Thomson et al., 2012) as characterized in Apen et al. (2022; lower intercept age of 467 ±  
205 9 Ma). Both MRC-1 (isochron age = 153.3 ± 0.2 Ma; Apen et al., 2022) and Mount McClure  
206 (common Pb corrected via total Pb-U isochron = 523.51 ± 1.53 Ma; Schoene & Bowring, 2006)  
207 apatite reference materials were analyzed as unknowns to assess reproducibility. Analyses of  
208 MRC-1 yielded lower intercept dates in Tera-Wasserburg space of 154 ± 1 Ma (mean squared  
209 weighted deviates [MSWD] = 1, n = 12/12), 155 ± 2 Ma (MSWD = 0.91, n = 14/15), 157 ± 2 Ma  
210 (MSWD = 1, n = 20/20), and 152 ± 2 Ma (MSWD = 1.7, n = 10/10). The two analytical runs that  
211 included Mount McClure apatite returned lower intercept dates of 522 ± 6 Ma (MSWD = 5.5, n  
212 = 14/15) and 531 ± 17 Ma (MSWD = 1.6, n = 19/20). With one exception, all analyses of apatite  
213 secondary reference materials overlap within uncertainty of expected ages; the one exception is  
214 within 1% of the expected age.

215 The reference materials used for titanite geochronology include MKED1, Mount  
216 McClure, and Mud Tank. MKED1 was used as the primary reference material for all titanite  
217 isotopic analyses ( $^{206}\text{Pb}/^{238}\text{U}$  age of  $1517.32 \pm 32$  Ma; Spandler et al., 2016). To assess the  
218 accuracy of the U-Pb results, the Mount McClure titanite reference material (common Pb  
219 corrected via total Pb-U isochron =  $523.26 \pm 0.72$  Ma; Schoene & Bowring, 2006) was analyzed  
220 as an unknown in five analytical sessions while the titanite reference material Mud Tank ( $318.7$   
221  $\pm 1.0$  Ma; Fisher et al., 2020) was used for the remaining three sessions. LA-ICP-MS analyses of  
222 Mount McClure titanite typically contain significant and variable common Pb contents. As such,  
223 lower intercept dates in Tera-Wasserburg space are used to assess how well the expected age was  
224 reproduced. Analyses of Mount McClure titanite yielded dates of  $522 \pm 3$  Ma (MSWD = 1.7, n =  
225 9/10),  $529 \pm 4$  (MSWD = 0.72, n = 5/5),  $523 \pm 14$  Ma (MSWD = 2.3, n = 6/6),  $522 \pm 12$  Ma  
226 (MSWD = 2.1, n = 8/8), and  $528 \pm 4$  Ma (MSWD = 1.3, n = 13/13). With one exception, all  
227 dates overlap the expected date within analytical uncertainty. The exception is well within  
228 (0.1%) the expected uncertainties associated with LA-ICP-MS U-Pb geochronology (e.g.,  
229 Horstwood et al., 2016). Analyses of Mud Tank titanite were essentially homogeneous with  
230 respect to common Pb, and as such,  $^{207}\text{Pb}$ -corrected (Stacey & Kramers, 1975)  $^{206}\text{Pb}/^{238}\text{U}$   
231 weighted mean dates were used to assess reproducibility. The three analytical runs with Mud  
232 Tank titanite yielded dates of  $319 \pm 1$  Ma (MSWD 2.9, n = 9/10),  $316 \pm 1$  Ma (MSWD 1.5, n =  
233 13/14) and  $316 \pm 1$  Ma (MSWD 1.2, n = 17/17). All Mud Tank results are within 0.3% of the  
234 expected date, again well-within expected reproducibility.

235 Glasses NIST 610 and NIST 612 were used as reference materials for trace element  
236 analyses for both apatite and titanite. Concentrations were normalized to assumed stoichiometric  
237 concentrations of Ca for apatite and Si for titanite. Trace element concentrations in secondary  
238 reference materials are typically within 5–15% of expected values, with Zr < 5%.

### 239 3.2 U-Pb data analysis

240 The LA-ICP-MS data were initially reduced using Iolite (Paton et al., 2011) to normalize  
241 down-hole fractionation and instrument drift over analytical runs. Excess dispersion in the  
242  $^{207}\text{Pb}/^{206}\text{Pb}$  and  $^{206}\text{Pb}/^{238}\text{U}$  ratios was calculated from secondary reference materials (e.g., Mount  
243 McClure, Mud Tank, MRC-1) and added to apatite and titanite analyses using in-house data  
244 processing scripts. Typical dispersion values were < 1.5%. Tera-Wasserburg diagrams and trace  
245 element plots were constructed using Chrontour (Larson, 2022) and DataGraph (Visual  
246 DataTools, 2021). When constructing Tera-Wasserburg diagrams for specimens with multiple  
247 populations, the intercept of a single regression through all included data was used for the  
248 individual regressions to be internally consistent. Uncertainties reported in-text and depicted in  
249 figures refer to internal (2 standard error; 2SE) uncertainties only.

### 250 3.3 Zirconium-in-titanite geothermometry

251 Zirconium (Zr) concentrations were measured in each titanite spot analysis and  
252 (re)crystallization temperatures were calculated using the Zr-in-titanite geothermometer of  
253 Hayden et al. (2008). The activities of titania ( $\text{TiO}_2$ ) and silica ( $\text{SiO}_2$ ) were assumed to be 0.8 and  
254 1.0, respectively; an activity of titania between 0.75–0.85 is considered an acceptable estimate  
255 for a wide range of metamorphic rocks (Kapp et al., 2009; Kohn, 2017). Recent estimates for the  
256 last recorded equilibrium conditions across most metamorphic units in the field area include  
257 pressures between approximately 0.4–0.7 GPa (Dyck et al., 2021). Because it is difficult to

258 determine the equilibrium mineral assemblage associated with titanite crystallization, as well as  
259 the lack of independent pressure constraints for the samples analyzed, we chose a value of 0.5  
260 GPa as the best approximation for pressure as it applies to the broadest range of samples.  
261 Temperatures calculated with the Zr-in-titanite geothermometer are only moderately pressure-  
262 dependent; a change in pressure of 0.1 GPa corresponds to a change in temperature of 10–13 °C  
263 for the grains analyzed. Uncertainties reported for temperatures in-text reflect the standard  
264 calibration uncertainty of  $\pm 20$  °C reported by Hayden et al. (2008).

## 265 4 Results

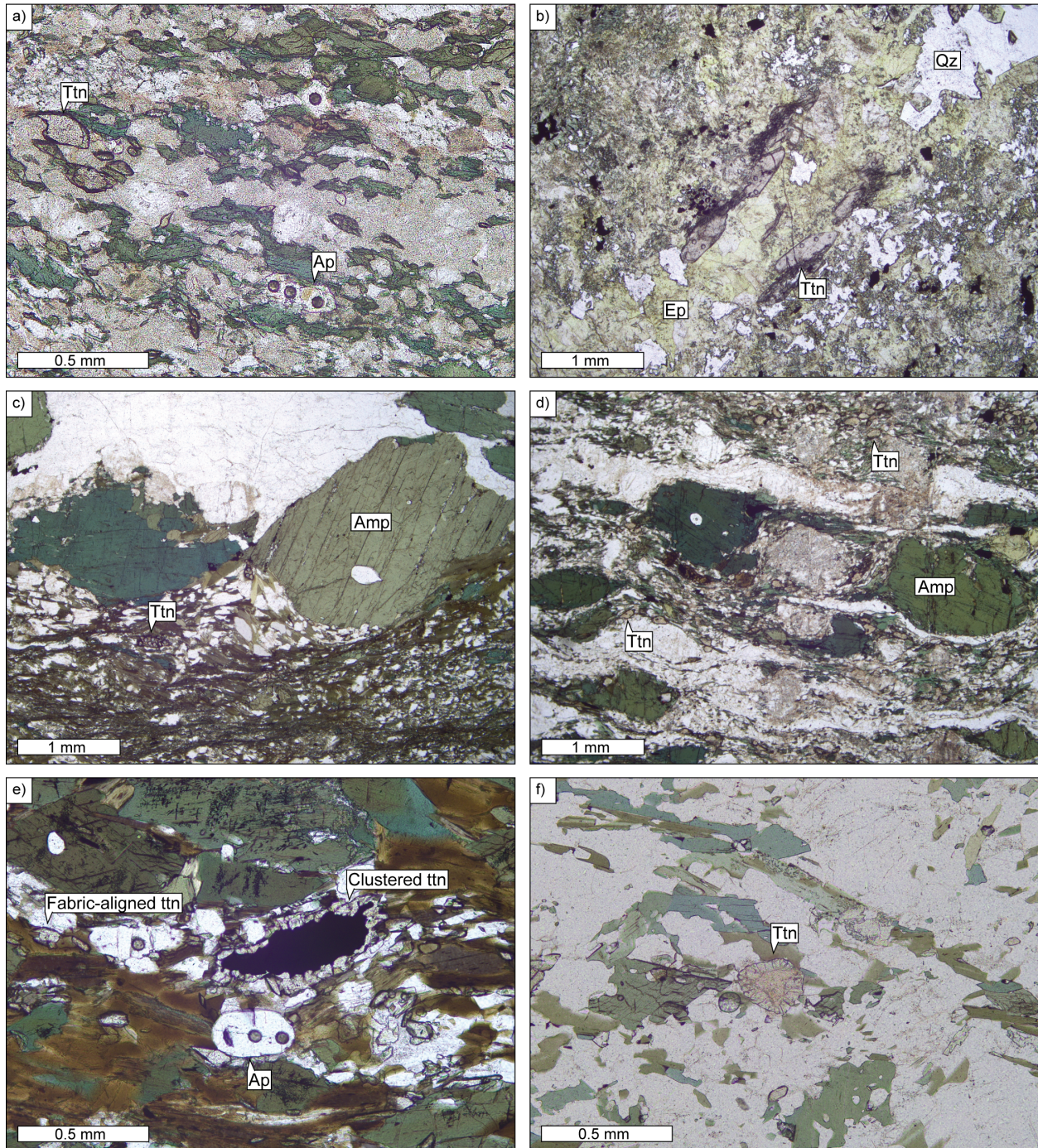
### 266 4.1 Sample petrography

267 Of the 11 samples selected for *in situ* U-Th-Pb accessory mineral petrochronology, 4  
268 were collected north of the Laloche River fault (GSL-18-BD07, GSL-21-DS07, GSL-18-BD27,  
269 GSL-18-C50) while the remaining 7 are from south of the fault (Fig. 1c). Detailed petrographic  
270 descriptions for all samples are presented in Text S1, photomicrographs of key microstructural  
271 features in Figure 2, and grain characteristics of apatite and titanite in Table 1.

272 The four samples collected in the northern structural domain exhibit broad ranges in  
273 degree of mylonitization, lithology, and metamorphic facies, with three samples (GSL-21-DS07,  
274 GSL-18-BD27, GSL-18-C50) of mylonitic schist and one (GSL-18-BD07) of ultramylonitic  
275 granodiorite. The preserved metamorphic facies in the four samples range from the greenschist  
276 facies (GSL-18-BD07) to the epidote-amphibolite (GSL-21-DS07, GSL-18-C50) and upper-  
277 amphibolite facies (GSL-18-BD27). Two of the samples (GSL-18-BD07, GSL-18-C50) contain  
278 both apatite and titanite, whereas the remaining two samples each contain only one of the  
279 minerals (titanite in GSL-21-DS07; apatite in GSL-18-BD27). Apatite and titanite occur  
280 primarily in the matrix of each sample and are aligned with the foliation (Fig. 2a). One exception  
281 is GSL-21-DS07, in which there is extensive evidence of late fluid alteration and titanite occurs  
282 predominantly along late, coarse-grained quartz-epidote veins (Fig. 2b). Another exception is  
283 GSL-18-C50, which consists of a very fine-grained mylonitic matrix that wraps large  
284 clinzoisite–amphibole–titanite pseudomorphs after garnet (Dyck et al., 2021). Most apatite and  
285 titanite grains in the sample occur within the garnet pseudomorph and are aligned oblique to the  
286 matrix foliation.

287 South of the Laloche River fault, six samples (GSL-21-DS14, GSL-18-BD11, GSL-21-  
288 DS16, GSL-21-DS18, GSL-18-BD24, GSL-21-DS20) were collected from the southern  
289 structural domain of the shear zone while the remaining sample (GSL-21-BD12) was collected  
290 from a supracrustal unit in the Rutledge Group south of the shear zone (Fig. 1c). Except for  
291 GSL-21-DS14 (greenschist facies), all samples collected from the southern structural domain  
292 preserve epidote-amphibolite facies mineral assemblages. Furthermore, all six samples exhibit  
293 similar mineralogy and microstructure, with one of the six (GSL-18-BD11) identified as a  
294 mylonitic granodiorite and the remaining five as amphibole mylonitic granodiorites. The sample  
295 collected south of the shear zone (GSL-21-BD12) stands apart as an upper-amphibolite facies  
296 amphibole schist. All samples exhibit a strong, anastomosing foliation that is defined by the  
297 orientation of matrix-forming minerals, usually amphibole or biotite, and by the alignment of  
298 quartz ribbons and micaceous layers. Each of the seven samples contains both apatite and  
299 titanite, the grains of which occur primarily in the mylonitic matrix and are well-aligned with the  
300 foliation (Figs. 2c & d). One sample (GSL-21-DS16) contains two titanite populations, identified

301 based on textural observations (Fig. 2e). The first population consists of sub- to anhedral titanite  
 302 grains that are well-aligned with the foliation (referred to as “fabric-aligned titanite”), while the  
 303 second consists of small, round titanite grains clustered together around long masses of ilmenite  
 304 (“clustered titanite”). Several samples contain titanite grains that exhibit distinct core-rim  
 305 structures (Fig. 2f).



306

307 **Figure 2.** Summary of microstructural characteristics of apatite- and titanite-bearing samples.  
 308 Mineral abbreviations follow Whitney and Evans (2010). (a) Well-aligned apatite and titanite

309 grains (GSL-18-BD07). (b) Titanite grains associated with late coarse-grained quartz-epidote  
310 vein (GSL-21-DS07). (c) Mylonitic fabric defined by fine-grained micaceous domains wrapping  
311 around amphibole porphyroclasts (GSL-21-DS14). (d) Well-developed foliation wrapping  
312 amphibole porphyroclasts (GSL-21-DS18). (e) Fabric-aligned and clustered titanite grains in  
313 GSL-21-DS16. (f) Core-rim structure visible in a titanite grain (GSL-18-BD24).

314 **Table 1.** Summary of apatite and titanite grain characteristics.

Sample	Latitude (degrees)	Longitude (degrees)	Mineral	Grain characteristics				
				Occurrence	Relationship to fabric	Size ( $\mu\text{m}$ )	Shape	Zoning
GSL-18-BD07	61.643778	-112.212944	Ap	Matrix	Aligned	50–100	Sub- to anhedral	Patchy core-rim
			Ttn	Matrix	Aligned	60–700	Elongate, sub- to euhedral	Homogeneous or irregular patchy
GSL-21-DS07	61.646371	-112.195418	Ttn	Along qz-ep veins	Not aligned	200–1000	Euhedral	Oscillatory
GSL-18-BD27	61.630500	-112.200944	Ap	Matrix + inclusions in grt	Varies	50–200	Rounded, subhedral	Homogeneous
GSL-18-C50	61.629250	-112.199889	Ap	Within grt pseudomorph (+ matrix)	Oblique (+ aligned)	50–400	Anhedral, fractured	Patchy or core-rim
			Ttn	Within grt pseudomorph	Oblique	100–800	Rhombic	Patchy or oscillatory
GSL-21-DS14	61.647845	-112.105861	Ap	Matrix	Aligned	60–500	Elongate	Patchy
			Ttn	Matrix	Aligned	50–200	Subhedral	Core-rim
GSL-18-BD11	61.629250	-112.167250	Ap	Matrix	Aligned	60–250	Elongate, sub- to anhedral	Oscillatory or core-rim
			Ttn	Matrix, along micaceous layers	Aligned	20–120	Blocky	Homogeneous

GSL-21-DS16	61.608126 -112.137535	Ap	Matrix, in amp-rich domains	Aligned	80–250	Rounded, elongate	Irregular core-rim
		Ttn	Fabric-aligned ttn: matrix	Aligned	25–120	Sub- to anhedral	Core-rim
			Clustered ttn: surrounding masses of ilm	Not aligned	25–120	Elongate clusters of rounded grains	Core-rim
GSL-21-DS18	61.585146 -112.177447	Ap	Matrix	Aligned	50–200	Elongate, sub- to euhedral	Patchy, uncommon bright cores
		Ttn	Matrix, often with bt	Aligned	50–350	Elongate, sub- to anhedral	Irregular patchy
GSL-18-BD24	61.600083 -112.089167	Ap	Matrix	Aligned	50–200	Elongate, sub- to euhedral	Patchy, uncommon bright cores
		Ttn	Matrix	Aligned	100–1500	Sub- to anhedral	Core-rim
GSL-21-DS20	61.561525 -112.139314	Ap	Matrix	Aligned	70–300	Elongate, sub- to euhedral	Irregular oscillatory
		Ttn	Matrix, often with amp + bt	Aligned	50–500	Rhombic	Homogeneous
GSL-21-BD12	61.530367 -112.034200	Ap	Matrix + inclusions in amp	Varies	50–200	Anhedral	Patchy core-rim
		Ttn	Matrix	Aligned	50–200	Blocky to anhedral	Patchy core-rim

315 **Note.** Samples are ordered geographically, NW to SE. Mineral abbreviations follow Whitney and Evans (2010).

## 316 4.2 Apatite U-Pb and trace element results

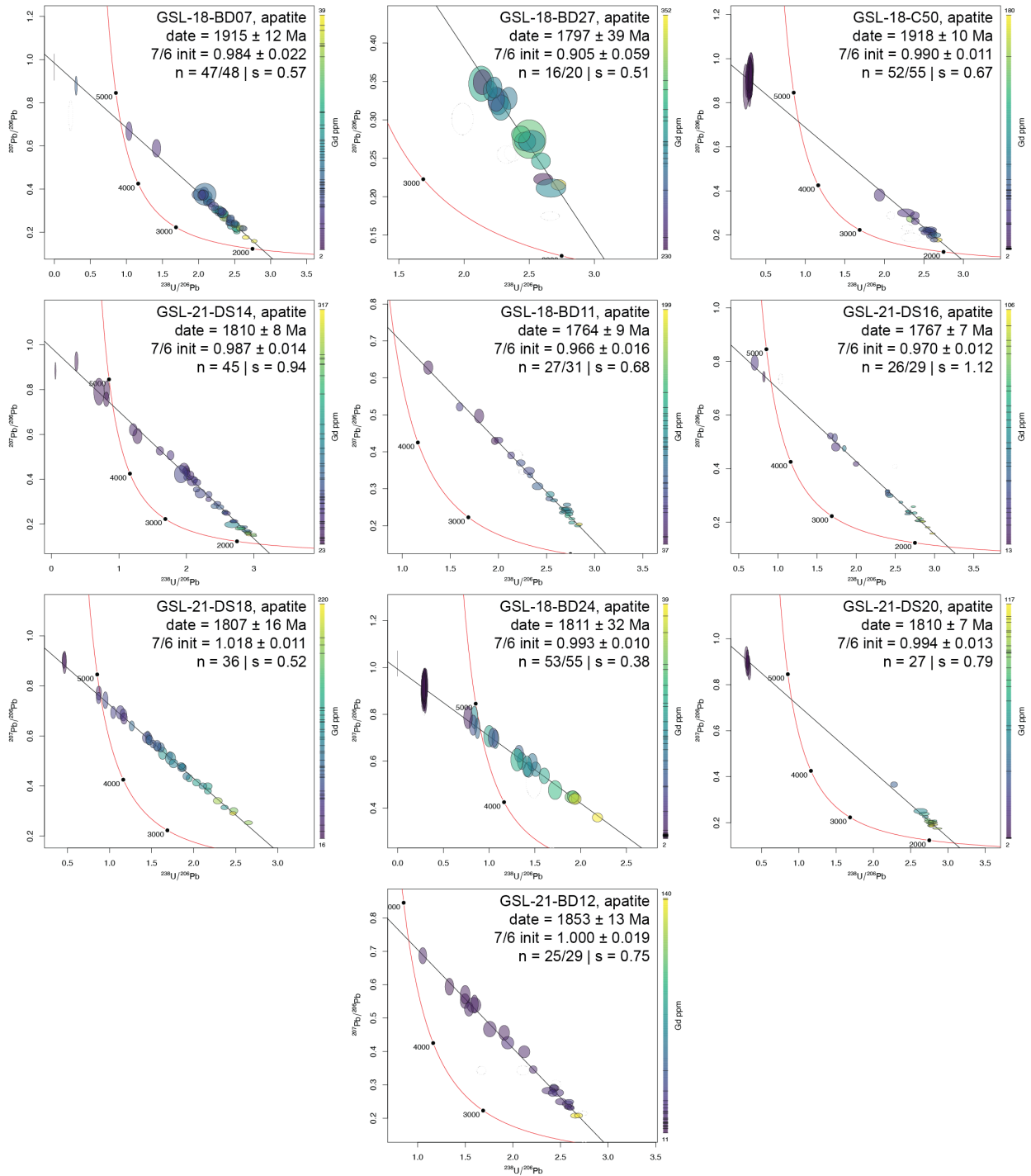
317 Tera-Wasserburg diagrams and representative REE profiles for all apatite populations are  
318 presented in Figures 3 and 4a, respectively. Detailed trace element plots as well as BSE and CL  
319 images of representative grains for all populations are presented in Figure S1 and full analytical  
320 results for all unknowns and reference materials are reported in Table S2. In the following text,  
321 unless otherwise specified, uncertainties reported refer to internal uncertainties only and do not  
322 reflect the externally reproducible uncertainties.

323 All apatite-bearing samples contain one main age population (Fig. 3). Lower intercept  
324 dates were calculated using the robust regression of Powell et al. (2020) for all populations and  
325 range from ca. 1920–1760 Ma. The oldest apatite populations are from samples collected north  
326 of the Laloche River fault and yield lower intercept dates of  $1918 \pm 10$  Ma (GSL-18-C50; spine  
327 width [s] = 0.67) and  $1915 \pm 12$  Ma (GSL-18-BD07; s = 0.57). The remainder of the apatite  
328 populations yield lower intercept dates between ca. 1860–1760 Ma.

329 Apatite spot analyses across all samples yield similar REE profiles with the main  
330 difference between analyses being the relative abundance of elements. Analyses that are  
331 classified as low-U analyses (<0.4 ppm) and that correspond to grains that disaggregated during  
332 ablation tend to exhibit the lowest overall concentrations of REE.

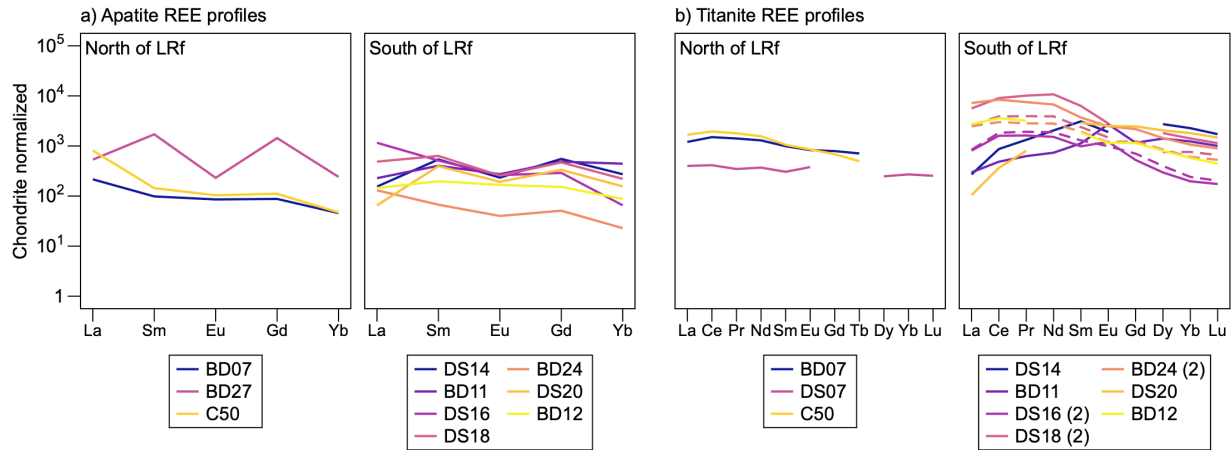
333 Four samples (GSL-18-BD27, GSL-21-DS14, GSL-21-DS18, GSL-21-DS20) exhibit  
334 depletion in Eu relative to Sm and Gd (Fig. 4a) with mean Eu/Eu\* ranging from 0.15–0.60, the  
335 greatest of which is recorded in GSL-18-BD27 (mean Eu/Eu\* = 0.15). There does not appear to  
336 be a correlation between Eu/Eu\* and other REE ratios.

337 Three samples (GSL-18-BD27, GSL-18-C50, GSL-21-DS16) exhibit significant  
338 enrichment of LREE relative to HREE (Fig. 4a), with mean  $La_n/Yb_n$  ranging from 16.79–17.76.  
339 Despite the similarities in relative LREE enrichment, these three samples exhibit distinct REE  
340 profiles. GSL-18-BD27 has a significant negative Eu anomaly, giving its REE profile a sawtooth  
341 appearance, while GSL-18-C50 and GSL-21-DS16 exhibit steadier decreases in REE  
342 concentration across their profiles, consistent with the overall enrichment of LREE relative to  
343 HREE observed (Fig. 4a). Five samples (GSL-18-BD07, GSL-21-DS18, GSL-18-BD24, GSL-  
344 21-DS20, GSL- 21-BD12) also exhibit enrichment of LREE relative to HREE (Fig. 4a), but  
345 record slightly lower mean  $La_n/Yb_n$ , with values ranging from 2.06–9.20. Meanwhile, the two  
346 remaining samples (GSL-21-DS14, GSL-18-BD11) exhibit an overall depletion of LREE  
347 relative to HREE (Fig. 4a), with mean  $La_n/Yb_n$  of 0.45 and 0.49, respectively.



348

349 **Figure 3.** Tera-Wasserburg diagrams for each apatite population, constructed using ChrontourR  
 350 (Larson, 2022). 7/6 init – initial  $^{207}\text{Pb}/^{206}\text{Pb}$  ratio.



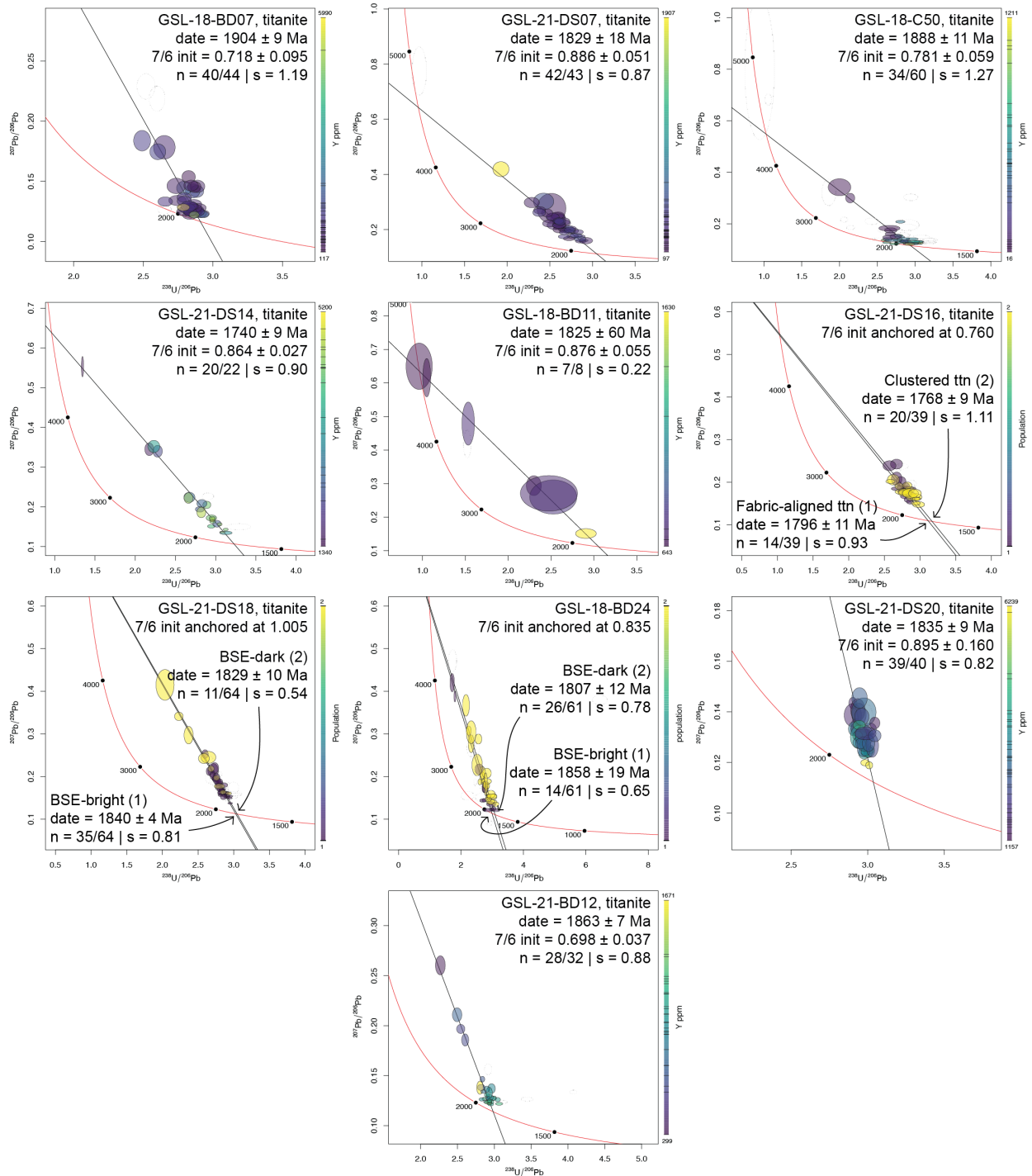
351

352 **Figure 4.** Average REE profiles for all apatite (a) and titanite (b) populations. All samples  
 353 contain one population of each mineral, except for DS16, DS18, and BD24, which each contain  
 354 two titanite populations; dashed lines indicate secondary populations (clustered titanite in DS16;  
 355 BSE-dark titanite in DS18, BD24). LRF – Laloche River fault.

#### 356 4.3 Titanite U-Pb and trace element results

357 Tera-Wasserburg diagrams and representative REE profiles for all titanite populations are  
 358 presented in Figures 5 and 4b, respectively. Detailed trace element plots and BSE images of  
 359 representative grains for all populations are presented in Figure S2 and full analytical results for  
 360 all unknowns and reference materials are reported in Table S3. As with the apatite data, unless  
 361 otherwise specified, uncertainties reported in-text refer to internal uncertainties only.

362 With the exceptions of GSL-18-BD24, GSL-21-DS16, and GSL-21-DS18, which each  
 363 contain two distinct populations characterized by differences in grain morphology and trace  
 364 element profiles, most titanite-bearing samples contain one main age population (Fig. 5). Lower  
 365 intercept dates were calculated for all populations and range from ca. 1910–1740 Ma across the  
 366 shear zone. The oldest titanite populations yield lower intercept dates of  $1904 \pm 9$  Ma (GSL-18-  
 367 BD07;  $s = 1.19$ ) and  $1888 \pm 11$  Ma (GSL-18-C50;  $s = 1.27$ ) and occur in the same two samples  
 368 that have the oldest apatite populations. Meanwhile, the youngest titanite populations are from  
 369 samples collected south of the Laloche River fault and yield lower intercept dates of  $1740 \pm 9$   
 370 Ma (GSL-21-DS14;  $s = 0.90$ ) and  $1768 \pm 9$  Ma (clustered titanite in GSL-21-DS16;  $s = 1.11$ ).  
 371 The remainder of the lower intercept dates fall between ca. 1870–1790 Ma.



372

373 **Figure 5.** Tera-Wasserburg diagrams for each titanite population, constructed using ChrontouR  
 374 (Larson, 2022). 7/6 init – initial  $^{207}\text{Pb}/^{206}\text{Pb}$  ratio.

375 Most analyses within individual samples have similar REE profiles with the main  
 376 difference between analyses being the relative abundance of elements. Seven populations (GSL-  
 377 21-BD12, two in GSL-18-BD24, two in GSL-21-DS16, two in GSL-21-DS18) exhibit strikingly  
 378 similar concave-down REE profiles that show an overall enrichment in LREE relative to HREE

379 (Fig. 4b). These samples record mean  $La_n/Lu_n$  ranging from 4.24–8.67. All seven populations  
 380 exhibit little to no enrichment of LREE relative to MREE, with mean  $La_n/Sm_n$  ranging from  
 381 0.67–2.11; however, all seven populations show enrichment of MREE relative to HREE, with  
 382 mean  $Sm_n/Lu_n$  ranging from 3.37–6.34. Three additional samples (GSL-21-DS14, GSL-18-  
 383 BD11, GSL-21-DS20) also have concave-down REE profiles but show an overall depletion in  
 384 LREE relative to HREE (Fig. 4b), with mean  $La_n/Lu_n$  ranging from 0.08–0.38. All three further  
 385 exhibit a depletion in LREE relative to MREE, with mean  $La_n/Sm_n$  ranging from 0.04–0.43, as  
 386 well as a relatively low enrichment of MREE relative to HREE, with mean  $Sm_n/Lu_n$  ranging  
 387 from 1.04–1.90. One sample (GSL-21-DS07) has a relatively flat REE profile compared to the  
 388 others (Fig. 4b), with a mean  $La_n/Lu_n$  of 1.71. The mean  $La_n/Sm_n$  and  $Sm_n/Lu_n$  are similarly  
 389 stable, with values of 1.43 and 1.23.

390 The REE profiles for the distinct age populations in GSL-18-BD24, GSL-21-DS16, and  
 391 GSL-21-DS18 differ. In GSL-21-DS16, most of the analyses from the fabric-aligned titanite  
 392 population exhibit enrichment in Eu relative to Sm and Gd, whereas there is no enrichment in Eu  
 393 in the analyses from the clustered titanite population (Fig. 4b). In GSL-18-BD24 and GSL-21-  
 394 DS18, the BSE-bright and BSE-dark populations exhibit similar overall patterns in REE profiles,  
 395 however, the BSE-dark analyses typically record lower REE concentrations than the analyses  
 396 from BSE-bright domains (Fig. 4b). For example, Sm concentrations in GSL-18-BD24 range  
 397 from 271–932 ppm (BSE-bright) compared with 49–606 ppm (BSE-dark), while in GSL-21-  
 398 DS18, they range from 328–1384 ppm (BSE-bright) compared with 146–812 ppm (BSE-dark).

#### 399 4.4 Zr-in-titanite thermometry

400 Zr-in-titanite temperatures were calculated for each of the titanite analyses following the  
 401 steps outlined by Hayden et al. (2008). Mean and median temperatures were calculated for each  
 402 titanite population. Mean temperatures are used for comparison between populations. A box-and-  
 403 whisker plot of temperatures calculated for each titanite population is presented in Figure 6 and  
 404 full results are reported in Table S4. Titanite records temperatures ranging from approximately  
 405 630–950 °C across all samples. Mean temperatures calculated for each of the thirteen titanite  
 406 populations range from  $674 \pm 20$  °C (GSL-21-DS07) up to  $768 \pm 20$  °C (GSL-18-C50).

## 407 5 Discussion

### 408 5.1 A temporal record of dynamic (re)crystallization

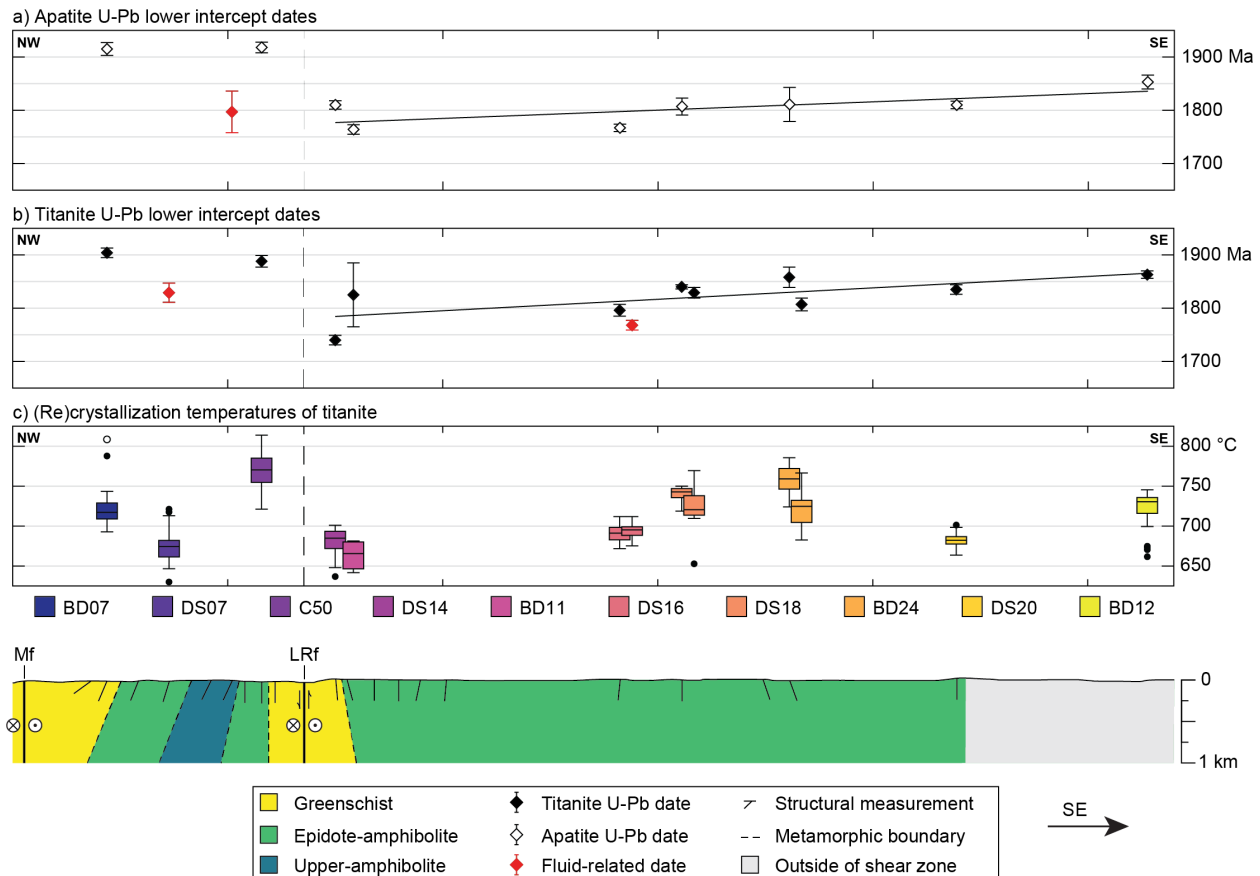
409 The lower intercept dates recorded by all apatite and titanite populations are plotted in  
 410 Figure 6 according to sample position along the transect of the study area. The apatite and  
 411 titanite chronometers yield overlapping ranges of dates across the shear zone, spanning from ca.  
 412 1920–1760 Ma and ca. 1910–1740 Ma, respectively. The range of dates recorded by both  
 413 chronometers post-date prograde-to-peak metamorphism in the shear zone as recorded by two  
 414 garnet Lu-Hf ages of  $1931 \pm 12$  and  $1917 \pm 6$  Ma and overlapping zircon and monazite ages (ca.  
 415 1933–1913 Ma; Cutts & Dyck, 2022). Furthermore, the dates yielded by apatite and titanite  
 416 south of the Laloche River fault (ca. 1860–1760 and ca. 1870–1740 Ma, respectively) post-date  
 417 the crystallization of plutonic host rocks within the shear zone ( $> 1930$  Ma; Cutts et al., 2022).  
 418 Together, these relationships indicate that the populations both north and south of the Laloche  
 419 River fault are unlikely to represent either a primary igneous or prograde metamorphic origin.

420 Both chronometers record older dates on the north side of the Laloche River fault (Fig. 6)  
421 with the oldest apatite and titanite dates occurring in the same two samples: GSL-18-BD07  
422 (apatite  $1915 \pm 12$  Ma; titanite  $1904 \pm 9$  Ma) and GSL-18-C50 (apatite  $1918 \pm 10$  Ma; titanite  
423  $1888 \pm 11$  Ma). Moreover, both chronometers demonstrate an overall younging trend toward the  
424 fault in the southern structural domain (Fig. 6). A similar pattern is also reflected in Zr-in-titanite  
425 temperatures, which exhibit an overall decrease from south of the study area towards the Laloche  
426 River fault (Fig. 6).

427 In all but three populations (GSL-21-BD27, GSL-21-DS07, clustered titanite in GSL-21-  
428 DS16), apatite and titanite grains have a shape-preferred orientation that is aligned with ductile  
429 shear fabrics (Figs. 2a, c & d). Considering these textural observations in conjunction with the  
430 timing and nature of apatite and titanite (re)crystallization in the shear zone, we interpret the  
431 apatite and titanite dates as recording syn-kinematic (re)crystallization, which encompasses both  
432 dynamic recrystallization of, or re-equilibration of the U-Pb system in, pre-existing apatite and  
433 titanite as well as syn-tectonic growth of new grains. It is possible that the apatite and titanite  
434 grains that are aligned with shear planes do not record the timing of the shear process (i.e., they  
435 record pre-shear (re)crystallization processes), however, given that the apatite and titanite data  
436 are significantly younger than prograde-to-peak metamorphism as outlined above, it is unlikely  
437 that these chronometers are recording earlier magmatic or metamorphic events. Moreover, given  
438 that apatite and titanite dates at similar structural positions typically overlap, we consider it  
439 unlikely that they are cooling ages. Apatite has a nominal closure temperature (in the sense of  
440 Dodson, 1973) of  $\sim 425\text{--}530$  °C (Chamberlain & Bowring, 2001; Cherniak et al., 1991) whereas  
441 recent estimates for titanite closure temperatures are much higher in excess of 700 °C (Gao et al.,  
442 2012; Kohn, 2017; Kohn & Corrie, 2011; Spencer et al., 2013; Stearns et al., 2015).

443 While most of the apatite and titanite populations are interpreted to record the timing of  
444 ductile shear, two titanite populations (GSL-21-DS07, clustered titanite in GSL-21-DS16) and  
445 one apatite population (GSL-18-BD27) exhibit distinct textural and geochemical characteristics  
446 that require additional explanation. Titanite grains in GSL-21-DS07 occur predominantly along  
447 late coarse-grained quartz-epidote veins (Fig. 2b) and exhibit oscillatory zoning in BSE (Fig  
448 S2b). Titanite also occurs in the heavily altered matrix of the sample. These grains display  
449 resorption textures and exhibit irregular, patchy zoning (Fig. S2b), which we interpret as textural  
450 evidence of fluid alteration. Analyses from the quartz-epidote vein-hosted grains yield flat REE  
451 profiles that are distinct from all other titanite populations (Fig. 4b). The lack of enrichment or  
452 depletion in any of the REE is consistent with titanite (re)crystallization occurring in a relatively  
453 isolated system, away from the presence of other REE-bearing minerals (e.g., allanite, garnet;  
454 Garber et al., 2017). This observation is consistent with the interpretation that titanite in this  
455 sample (re)crystallized due to the fluid infiltration that resulted in the formation of quartz-epidote  
456 veins. Meanwhile, the clustered titanite in GSL-21-DS16 are differentiated from the fabric-  
457 aligned titanite in this sample by the absence of a strong positive Eu anomaly in their  
458 geochemical signature (Fig. 4b). The positive Eu anomaly exhibited by the fabric-aligned titanite  
459 is interpreted as indicating (re)crystallization coeval with plagioclase breakdown (e.g., Garber et  
460 al., 2017). Given the geochemical differences between the two populations and the lack of  
461 alignment of the clustered titanite with the mylonitic fabric (Fig. 2e), we interpret the clustered  
462 titanite as reflecting post-kinematic (re)crystallization in a plagioclase-free environment. Finally,  
463 the apatite population in GSL-18-BD27 yields a distinct REE profile with an overall enrichment  
464 in REE and a pronounced negative Eu anomaly (Fig. 4a). These geochemical characteristics have  
465 been previously interpreted to reflect hydrothermal alteration of apatite (e.g., Adlakha et al.,

466 2018), and while the specific effects of a fluid on apatite REE chemistry may vary between  
 467 localities, various studies have demonstrated the sensitivity of apatite trace element systematics  
 468 to hydrothermal activity (e.g., Bouzari et al., 2016; Mao et al., 2016; Ribeiro et al., 2020).  
 469 Furthermore, although apatite in this sample occurs both in the matrix and as inclusions in  
 470 garnet, both types of apatite record matching REE signatures (Fig. 4a), which is consistent with  
 471 all apatite grains re-equilibrating with a fluid.



472

473 **Figure 6.** Summary of petrochronology results plotted along the transect of the study area (Fig.  
 474 1c). The McDonald fault (Mf) and the Laloche River fault (LRf) are marked and the position of  
 475 the Laloche River fault is indicated on the plots by a dashed line. The horizontal position of each  
 476 marker corresponds to its approximate position along the transect. (a) Lower intercept dates of  
 477 apatite with  $2\sigma$  error bars. A linear fit to the data in the southern structural domain indicates a  
 478 faultward younging trend. (b) Lower intercept dates of titanite with  $2\sigma$  error bars. A linear fit to  
 479 the data in the southern structural domain (excluding clustered titanite in GSL-21-DS16)  
 480 indicates a faultward younging trend. (c) Box and whisker plot of the titanite (re)crystallization  
 481 temperatures, calculated using the geothermometer of Hayden et al. (2008). Outliers are  
 482 indicated by solid and open circles, which correspond to values larger than 1.5 and 3x the  
 483 interquartile range, respectively.

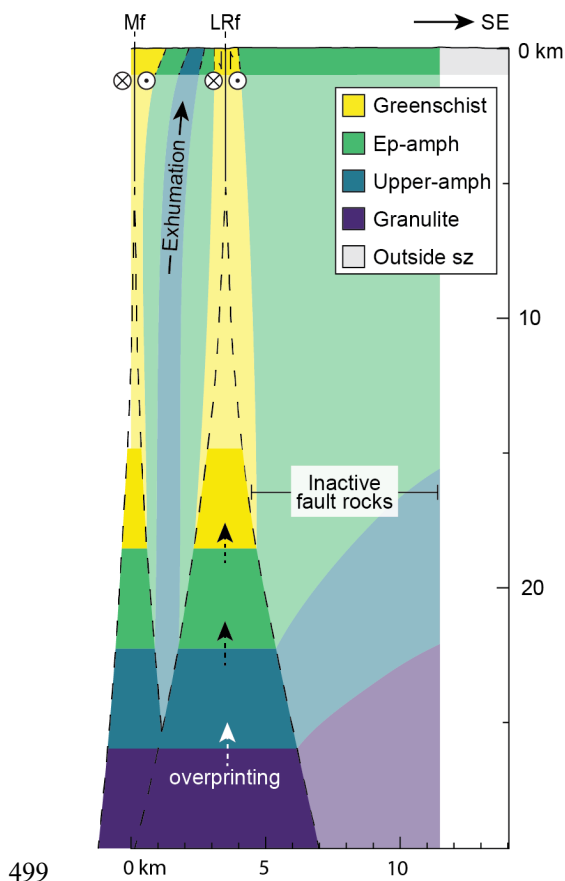
484

## 5.2 Architecture and temporal evolution of the GSLsz

485

486 Figure 7 presents a simplified model of the GSLsz. This model builds on basic Sibson-Scholz shear zone models, which consist of a zone of active deformation that is narrow near the

487 surface and broadens with depth, giving it a characteristic triangular shape (Scholz, 1988). In the  
 488 upper crust, deformation is dominated by brittle processes and strain is localized along one or  
 489 more discrete fault surfaces, whereas in the middle to lower crust, there is a gradual transition  
 490 from brittle to ductile processes and strain is distributed across a broadening zone of  
 491 deformation. One key prediction of the Sibson-Scholz model is the overprinting of higher-grade  
 492 metamorphic mineral assemblages by lower-grade ones, which is observed in all units of the  
 493 GSLsz. This overprinting is the result of the crust being exhumed and consequently experiencing  
 494 decreases in both pressure and temperature, reflected by changes in the stable mineral  
 495 assemblage. Because the metamorphic conditions preserved at the surface level of the GSLsz  
 496 reflect the lowest-grade mineral assemblages associated with ductile fabrics, the observed  
 497 metamorphic grade can be used to estimate depth at which a package of crustal material exited  
 498 the zone of active shear.



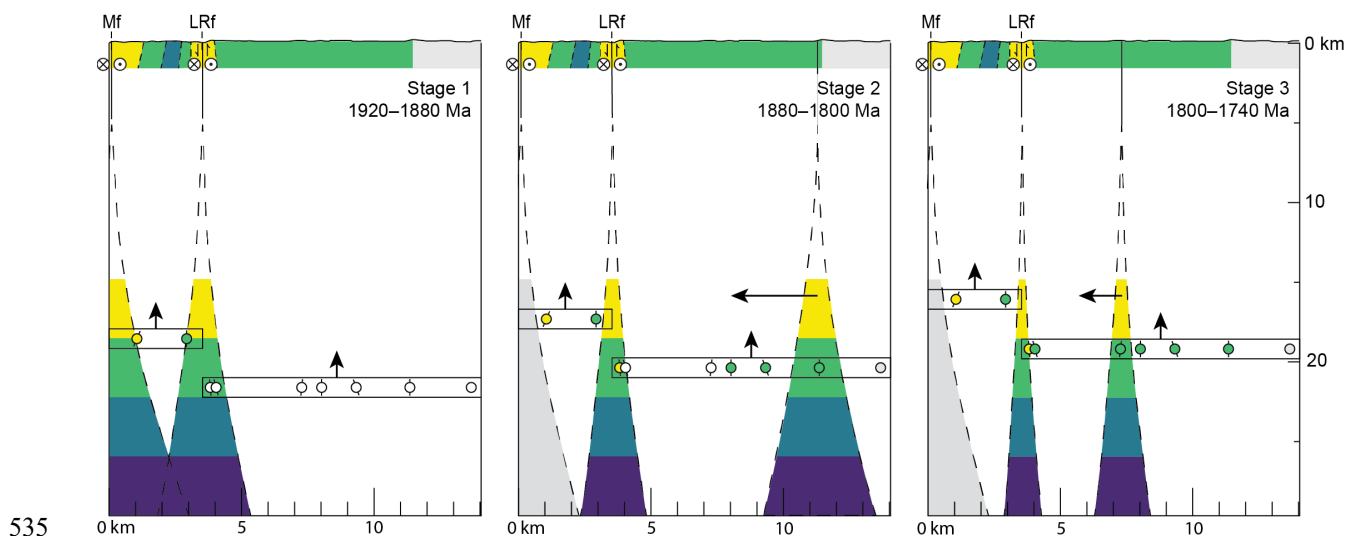
500 **Figure 7.** Two-strand shear zone model proposed for the GSLsz. The McDonald fault (Mf) and  
 501 the Laloche River fault (LRf) are marked. The zones of active deformation are outlined by  
 502 dashed lines. Gs refers to greenschist facies, Ep-amph to epidote-amphibolite facies, and upper-  
 503 amph to upper-amphibolite facies.

504 Our simplified model of the GSLsz adopts the peak thermal gradient of  $\sim 1000$  °C/GPa  
 505 reported by Dyck et al. (2021), which is based on petrological modelling of units from the  
 506 northern structural domain. Using this thermal gradient, the depths corresponding to key thermal  
 507 boundaries between metamorphic facies are estimated by assuming an average overburden  
 508 density of  $2750 \text{ kg/m}^3$ . The following thermal boundaries are assumed: (1) greenschist facies

509 corresponds to the temperature range of 400–500 °C, (2) epidote-amphibolite facies to 500–600  
 510 °C, (3) upper-amphibolite facies to 600–700 °C, and (4) granulite facies to 700–800 °C (Palin &  
 511 Dyck, 2021). The depths calculated for the thermal boundaries are used to define the vertical  
 512 extent of metamorphic layers in the shear zone.

513 Based on the observed symmetry of the metamorphic units exposed between the  
 514 McDonald and Laloche River faults, we propose that the GSLsz initially had two simultaneously  
 515 active strands of deformation, with one centered on the McDonald fault and the other centered on  
 516 the Laloche River fault (Fig. 7). As the width of the actively deforming region narrowed  
 517 structurally upward, a symmetrical pattern would have developed with respect to the most recent  
 518 recorded conditions of metamorphism and shear-(re)crystallization. The two greenschist facies  
 519 belts and neighboring epidote-amphibolite rocks that are centered on the McDonald and Laloche  
 520 River faults are consistent with progressive localization of strain along these structures.

521 Figure 8 presents a kinematic model for the GSLsz that builds on the two-strand model  
 522 presented in Figure 7. By using the apatite ages as a record of the time at which a sample exited  
 523 the actively deforming shear zone (and stopped (re)crystallizing), we estimate both the position  
 524 and width of the zones of active deformation over time. We propose three main stages for the  
 525 temporal evolution of the GSLsz (Fig. 8). In stage 1 (ca. 1920–1880 Ma), there are two strands  
 526 of active deformation centered on the McDonald and Laloche River faults. In stage 2 (ca. 1880–  
 527 1800 Ma), ductile deformation associated with the McDonald fault ceases and the locus of  
 528 deformation shifts southwards towards the Laloche River fault and one (or more) parallel strands  
 529 operating to the south of the Laloche River fault. During stage 3 (ca. 1800–1740 Ma), the active  
 530 deformation south of the Laloche River fault migrates northward, leaving no lower-grade brittle  
 531 record to the south of the fault. From the lack of variability in metamorphic grade on the south  
 532 side of the Laloche River fault, we interpret that the localization of shear along the fault occurred  
 533 while the now present-day surface was 15–20 km deep, and still below the base of the  
 534 seismogenic crust.



536 **Figure 8.** Tectonic model for the GSLsz. Colors correspond to metamorphic facies: yellow to  
 537 greenschist, green to epidote-amphibolite, blue to upper-amphibolite, purple to granulite. A  
 538 thermal gradient of 1000 °C/GPa is assumed for all stages. Apatite samples are indicated by  
 539 circles. Colored circles indicate samples that have exited the actively deforming shear zone by

540 the end of each stage. Arrows illustrate the exhumation of crustal layers as well as the lateral  
541 migration of the actively deforming strands over time. The McDonald fault (Mf) and Laloche  
542 River fault (LRf) are marked in each panel.

543 Our kinematic model (Fig. 8) involves a broad width of crust that was last deformed  
544 under epidote-amphibolite facies conditions. The active shear zone may have significantly  
545 widened when the stress that was originally accommodated by the McDonald fault is transferred  
546 southwards into the Rae craton. The Rae cratonic margin would have been relatively young at  
547 the time when the GSLsz was developed with voluminous Talston age (1.99–1.92 Ga) plutonism  
548 making up the bulk of the leading edge of the craton. It is possible that the (then) recent  
549 magmatism would contribute to an elevated crustal thermal gradient and a less-competent Rae  
550 margin. Along similar lines, the higher peak-metamorphic conditions and crustal thickening  
551 recorded in the northern domain may have led to a dehydrated and more competent Slave  
552 margin.

553 Over the span of 50 to 100 Myr, it is possible that an actively deforming strand shifted  
554 laterally by up to 10 km. In our model, the loci of shear shifted back towards the Laloche River  
555 fault and the McDonald fault upon exhumation. Therefore, the only evidence of localized, low-  
556 grade deformation has been lost due to the erosion of the upper-crustal expressions of these  
557 structures. The migration of the actively deforming strands over time does not change the  
558 interpretation that the strands decrease in width and range over time.

559 The presence of multiple active strands within major shear zones, as well as the lateral  
560 migration of these actively deforming strands, has been documented in modern-day analogues.  
561 The Karakoram fault zone in southwestern Tibet is known to have had several active fault  
562 strands throughout its history with varying amounts of slip occurring along each of these  
563 structures (e.g., Searle, 1996; Dunlap et al., 1998; Phillips et al., 2004). The North Anatolian  
564 fault zone in Turkey provides another example of a major strike-slip fault system consisting of  
565 multiple active branches (e.g., Okay et al., 1999; Hejl et al., 2010). Yet another well-known  
566 example would be the San Andreas fault system, which consists of over a dozen faults that all  
567 record distinct but often overlapping slip histories (e.g., Scharer and Streig, 2019). Each of these  
568 major transform systems yields extensive evidence of seismic activity along both main and  
569 subsidiary structures, a phenomenon that likely applied to the GSLsz as well.

570 Our model highlights several key observations, including the discrepancy in ages  
571 recorded across the Laloche River fault (Fig. 8). We posit that the Laloche River fault represents  
572 a much more significant tectonic boundary than previously thought. Both the apatite and titanite  
573 chronometers record significantly older ages of dynamic (re)crystallization on the north side of  
574 the Laloche River fault, while on the south side of the fault, they record younger ages that define  
575 a younging trend towards the centre of the shear zone. There may be several contributing factors  
576 that explain the age and depth discrepancy recorded across the fault, including: 1) a component  
577 of dip-slip motion along the Laloche River fault, resulting in the vertical juxtaposition of units of  
578 different ages; 2) the Laloche River fault represents a major tectonic boundary with inherent  
579 differences in rheology; and 3) there was an increased crustal thermal gradient in the southern  
580 structural domain at the time of deformation.

581 If the first explanation for the age discrepancy holds true, then the age difference  
582 recorded across the Laloche River fault could be the result of a north side-down component of  
583 dip-slip motion along the fault. Hanmer (1988) and Dyck et al. (2021) report evidence of a

584 shallow north side-down dip-slip component along the Laloche River fault, including mineral  
585 lineations and slickenlines along splay fault surfaces. Using the estimates of sample depth from  
586 the kinematic model, approximately 2–5 km of dip-slip motion would be required to bring all the  
587 samples to the same structural level.

588 The second explanation for the age discrepancy, which is that the Laloche River fault  
589 represents the suture between the Rae and Slave cratons, assumes a difference in crustal affinity  
590 across the boundary. This interpretation is consistent with lithological differences found across  
591 the shear zone. Recent work focusing on the plutonic rocks hosting the GSLsz has revealed  
592 distinct geochemical and geochronological signatures in zircon on either side of the Laloche  
593 River fault (Cutts et al., 2022). To the north of the fault, zircon preserve Archean ages and  
594 mantle oxygen isotope compositions, while to the south, they are Proterozoic in age and preserve  
595 heavier oxygen isotope compositions (Cutts et al., 2022). Additionally, mylonitic rocks on the  
596 south side of the Laloche River fault appear to reflect a broadly homogeneous deformation event,  
597 with minimal variation in the developed resultant textures and mineral assemblages, while those  
598 found north of the Laloche River fault preserve broad ranges in degree of mylonitization as well  
599 as metamorphic conditions, which extend up to granulite facies. There is a notable lack of  
600 evidence for high-pressure (>1 GPa), migmatization, and granulite facies metamorphism to the  
601 south of the fault (Dyck et al., 2021). Another key difference across the Laloche River fault is the  
602 presence of metasedimentary lithologies to the north of the fault, whereas none have been  
603 documented on the south side, indicating contrasting lithotectonic architectures. Together, these  
604 lines of evidence point to a difference in crustal affinity across the Laloche River fault consistent  
605 with the Laloche River fault representing the suture between the Rae and Slave cratons.

606 The third explanation for the age discrepancy involves a difference in crustal thermal  
607 gradient across the Laloche River fault. A modest increase in the thermal gradient of the southern  
608 structural domain, from 1000 to ~1100 °C/GPa, would reconcile the apparent differences in  
609 recrystallization depths at any given time. With the younger ages found only to south of the fault,  
610 there is no need for a step-change in temperatures across the fault. Instead, the entire shear zone  
611 could have experienced heating as it matured.

612 Considering the apatite and titanite ages in the context of the Rae-Slave suture, we  
613 interpret the older ages on the north side of the suture as recording the initial stages of strike-slip  
614 deformation related to the oblique collision between the Rae and Slave cratons. We interpret the  
615 ages on the south side of the suture as the broad-scale deformational response of the western Rae  
616 cratonic margin to the convergence and subsequent transform motion along the cratonic  
617 boundary. As there are no younger ages related to ductile deformation on the north side of the  
618 suture, the Slave craton likely remained relatively stable and rigid following its response to the  
619 initial collision, whereas the younger and weaker Rae cratonic margin continued to  
620 accommodate the bulk of the deformation related to the convergence.

## 621 **6 Conclusions**

622 We present *in situ* U-Pb geochronology results for the shear-induced (re)crystallization of  
623 apatite and titanite, which yield new information on the timing and duration of ductile  
624 deformation along the GSLsz and record a near-continuous history of ductile shear spanning ca.  
625 1920–1740 Ma. Based on the integration of this new geochronological data with structural and  
626 metamorphic observations across the structure, we propose a time-dependent kinematic model  
627 for the GSLsz that involves three stages of evolution. During stage 1 (ca. 1920–1880 Ma),

628 ductile shear is localized along two strands of active deformation in the northern structural  
 629 domain, centered on the McDonald and Laloche River faults. Stage 2 (ca. 1880–1800 Ma)  
 630 involves the cessation of shear along the McDonald fault and the migration of the locus of  
 631 deformation into the southern structural domain. Finally, during stage 3 (ca. 1800–1740 Ma),  
 632 deformation localizes back along the Laloche River fault. These interpretations reveal further  
 633 complexities in the case of the GSLsz, including the posited presence of the Slave-Rae suture  
 634 along the Laloche River fault, as supported by other lithological and geochemical work, and the  
 635 significance of the lateral migration of the zone of active deformation in major crustal shear  
 636 zones. Our results illustrate the necessity of providing structural and metamorphic context for  
 637 geochronological data to accurately constrain the evolution of crustal-scale structures and we  
 638 believe that the approach outlined here is widely applicable to other continental transform  
 639 systems.

## 640 **Acknowledgments**

641 We respectfully acknowledge the unceded traditional territories of the Dene peoples,  
 642 including the Łútsël K'é (Lutsel K'e) and the Deninu Kųę (Deninu Kue) First Nations, on which  
 643 we conducted fieldwork. We thank Mark Button, Sudip Shrestha and Dan Gibson for their  
 644 technical support and Alix Osinchuk and Rebecca Canam for fieldwork support. Funding for this  
 645 study was provided by a Natural Sciences and Engineering Research Council (NSERC) graduate  
 646 scholarship awarded to DS, a NSERC Discovery Grant awarded to BD, as well as support from  
 647 Natural Resource Canada's Polar Continental Shelf and GEM Geoscience programs.  
 648

## 649 **Open Research**

650 All U-Pb isotope and trace element data used in this manuscript are available in  
 651 Supplementary Tables S2–S4 and are also available from the Open Science Framework online  
 652 repository via <https://doi.org/10.17605/OSF.IO/WP3XQ> (Šilerová et al., 2022).  
 653

## 654 **References**

- 655 Adlakha, E., Hanley, J., Falck, H., & Boucher, B. (2018). The origin of mineralizing  
 656 hydrothermal fluids recorded in apatite chemistry at the Cantung W–Cu skarn deposit,  
 657 NWT, Canada. *European Journal of Mineralogy*, *30*(6), 1095–1113.  
 658 <https://doi.org/10.1127/ejm/2018/0030-2780>
- 659 Apen, F. E., Wall, C. J., Cottle, J. M., Schmitz, M. D., Kylander-Clark, A. R. C., & Seward, G.  
 660 G. E. (2022). Apatites for destruction: Reference apatites from Morocco and Brazil for U-  
 661 Pb petrochronology and Nd and Sr isotope geochemistry. *Chemical Geology*, *590*,  
 662 120689. <https://doi.org/10.1016/j.chemgeo.2021.120689>
- 663 Berman, R. G., Davis, W. J., Sanborn-Barrie, M., Whalen, J. B., Taylor, B. E., McMartin, I.,  
 664 McCurdy, M. W., Mitchell, R. K., Ma, S., Coyle, M., Roberts, B., & Craven, J. A.  
 665 (2018). Report of activities for the GEM-2 Chantrey-Thelon activity: Thelon Tectonic  
 666 Zone project, Nunavut. *Geological Survey of Canada*. <https://doi.org/10.4095/306622>
- 667 Bethune, K. M., Berman, R. G., Rayner, N., & Ashton, K. E. (2013). Structural, petrological and  
 668 U–Pb SHRIMP geochronological study of the western Beaverlodge domain: Implications  
 669 for crustal architecture, multi-stage orogenesis and the extent of the Taltson orogen in the

- 670 SW Rae craton, Canadian Shield. *Precambrian Research*, 232, 89–118.  
671 <https://doi.org/10.1016/j.precamres.2013.01.001>
- 672 Bostock, H. H., & Loveridge, W. D. (1988). Geochronology of the Taltson Magmatic Zone and  
673 its eastern cratonic margin, District of Mackenzie. *Radiogenic Age and Isotopic Studies:  
674 Report 2; Geological Survey of Canada, Paper no. 88-2*, 59–65.  
675 <https://doi.org/10.4095/126603>
- 676 Bostock, H. H., van Breemen, O., & Loveridge, W. D. (1987). Proterozoic geochronology in the  
677 Taltson Magmatic Zone, N.W.T. *Radiogenic Age and Isotopic Studies: Report 1;  
678 Geological Survey of Canada, Paper no. 87-2*, 73–80. <https://doi.org/10.4095/122751>
- 679 Bostock, H. H., van Breemen, O., & Loveridge, W. D. (1991). Further geochronology of  
680 plutonic rocks in northern Taltson Magmatic Zone, District of Mackenzie, N.W.T.  
681 *Radiogenic Age and Isotopic Studies: Report 4; Geological Survey of Canada, Paper no.  
682 90-2*, 67–78. <https://doi.org/10.4095/131938>
- 683 Bouzari, F., Hart, C. J. R., Bissig, T., & Barker, S. (2016). Hydrothermal alteration revealed by  
684 apatite luminescence and chemistry: A potential indicator mineral for exploring covered  
685 porphyry copper deposits. *Economic Geology*, 111(6), 1397–1410.  
686 <https://doi.org/10.2113/econgeo.111.6.1397>
- 687 Bowring, S. A., Schmus, W. R. V., & Hoffman, P. F. (1984). U–Pb zircon ages from  
688 Athapuscow aulacogen, East Arm of Great Slave Lake, N.W.T., Canada. *Canadian  
689 Journal of Earth Sciences*, 21(11), 1315–1324. <https://doi.org/10.1139/e84-136>
- 690 Cawood, T. K., & Platt, J. P. (2021). What controls the width of ductile shear zones?  
691 *Tectonophysics*, 816, 229033. <https://doi.org/10.1016/j.tecto.2021.229033>
- 692 Chacko, T., De, S. K., Creaser, R. A., & Muehlenbachs, K. (2000). Tectonic setting of the  
693 Taltson magmatic zone at 1.9–2.0–Ga: A granitoid-based perspective. *Canadian Journal  
694 of Earth Sciences*, 37(11), 1597–1609. <https://doi.org/10.1139/e00-029>
- 695 Chamberlain, K. R., & Bowring, S. A. (2001). Apatite–feldspar U–Pb thermochronometer: A  
696 reliable, mid-range (~450°C), diffusion-controlled system. *Chemical Geology*, 172(1),  
697 173–200. [https://doi.org/10.1016/S0009-2541\(00\)00242-4](https://doi.org/10.1016/S0009-2541(00)00242-4)
- 698 Cherniak, D. J., Lanford, W. A., & Ryerson, F. J. (1991). Lead diffusion in apatite and zircon  
699 using ion implantation and Rutherford Backscattering techniques. *Geochimica et  
700 Cosmochimica Acta*, 55(6), 1663–1673. [https://doi.org/10.1016/0016-7037\(91\)90137-T](https://doi.org/10.1016/0016-7037(91)90137-T)
- 701 Cutts, J. A., Dyck, B., Davies, J., & Stern, R. (2022). Tectonic setting and provenance of  
702 plutonic rocks hosting the Great Slave Lake shear zone from microanalytical zircon U-Pb  
703 geochronology and oxygen and hafnium isotopes. *GAC-MAC-IAH-CNC-CSPG 2022  
704 Halifax Meeting: Abstracts*, 45, 94. <https://doi.org/10.12789/geocanj.2022.49.188>
- 705 Cutts, J. A., & Dyck, B. (2022). Incipient collision of the Rae and Slave cratons at ca. 1.95 Ga.  
706 *GSA Bulletin*. <https://doi.org/10.1130/B36393.1>
- 707 Dunlap, W. J., Weinberg, R. F., & Searle, M. P. (1998). Karakoram fault zone rocks cool in two  
708 phases. *Journal of the Geological Society*, 155(6), 903–912.  
709 <https://doi.org/10.1144/gsjgs.155.6.0903>

- 710 Dyck, B., Goddard, R. M., Wallis, D., Hansen, L. N., & Martel, E. (2021). Metamorphic  
711 evolution of the Great Slave Lake shear zone. *Journal of Metamorphic Geology*, *39*(5),  
712 567–590. <https://doi.org/10.1111/jmg.12576>
- 713 Fisher, C. M., Bauer, A. M., Luo, Y., Sarkar, C., Hanchar, J. M., Vervoort, J. D., Tapster, S. R.,  
714 Horstwood, M., & Pearson, D. G. (2020). Laser ablation split-stream analysis of the Sm-  
715 Nd and U-Pb isotope compositions of monazite, titanite, and apatite – Improvements,  
716 potential reference materials, and application to the Archean Saglek Block gneisses.  
717 *Chemical Geology*, *539*, 119493. <https://doi.org/10.1016/j.chemgeo.2020.119493>
- 718 Gao, X.-Y., Zheng, Y.-F., Chen, Y.-X., & Guo, J. (2012). Geochemical and U–Pb age  
719 constraints on the occurrence of polygenetic titanites in UHP metagranite in the Dabie  
720 orogen. *Lithos*, *136–139*, 93–108. <https://doi.org/10.1016/j.lithos.2011.03.020>
- 721 Garber, J. M., Hacker, B. R., Kylander-Clark, A. R. C., Stearns, M., & Seward, G. (2017).  
722 Controls on trace element uptake in metamorphic titanite: Implications for  
723 petrochronology. *Journal of Petrology*, *58*, 1031–1057. doi:10.1093/petrology/egx046
- 724 Gibb, R. A., & Thomas, M. D. (1977). The Thelon front: A cryptic suture in the Canadian  
725 Shield? *Tectonophysics*, *38*(3–4), 211–222. [https://doi.org/10.1016/0040-1951\(77\)90211-](https://doi.org/10.1016/0040-1951(77)90211-6)  
726 [6](https://doi.org/10.1016/0040-1951(77)90211-6)
- 727 Gordon, S. M., Kirkland, C. L., Reddy, S. M., Blatchford, H. J., Whitney, D. L., Teyssier, C.,  
728 Evans, N. J., & McDonald, B. J. (2021). Deformation-enhanced recrystallization of  
729 titanite drives decoupling between U-Pb and trace elements. *Earth and Planetary Science*  
730 *Letters*, *560*, 116810. <https://doi.org/10.1016/j.epsl.2021.116810>
- 731 Hanmer, S. (1988). Great Slave Lake Shear Zone, Canadian Shield: Reconstructed vertical  
732 profile of a crustal-scale fault zone. *Tectonophysics*, *149*(3–4), 245–264.  
733 [https://doi.org/10.1016/0040-1951\(88\)90176-X](https://doi.org/10.1016/0040-1951(88)90176-X)
- 734 Hanmer, S., Bowring, S., van Breemen, O., & Parrish, R. (1992). Great Slave Lake shear zone,  
735 NW Canada: Mylonitic record of Early Proterozoic continental convergence, collision and  
736 indentation. *Journal of Structural Geology*, *14*(7), 757–773.  
737 [https://doi.org/10.1016/0191-8141\(92\)90039-Y](https://doi.org/10.1016/0191-8141(92)90039-Y)
- 738 Hanmer, S., & Lucas, S. B. (1985). Anatomy of a ductile transcurrent shear: The Great Slave  
739 Lake Shear Zone, District of Mackenzie, NWT (preliminary report). *Current Research*  
740 *Part B; Geological Survey of Canada, Paper no. 85-1B*, 7–22.  
741 <https://doi.org/10.4095/120223>
- 742 Hayden, L. A., Watson, E. B., & Wark, D. A. (2008). A thermobarometer for sphene (titanite).  
743 *Contributions to Mineralogy and Petrology*, *155*(4), 529–540.  
744 <https://doi.org/10.1007/s00410-007-0256-y>
- 745 Hejl, E., Bernroider, M., Parlak, O., & Weingartner, H. (2010). Fission-track thermochronology,  
746 vertical kinematics, and tectonic development along the western extension of the North  
747 Anatolian Fault zone. *Journal of Geophysical Research: Solid Earth*, *115*(B10).  
748 <https://doi.org/10.1029/2010JB007402>
- 749 Hoffman, P. F. (1987). Continental transform tectonics: Great Slave Lake shear zone (ca. 1.9  
750 Ga), northwest Canada. *Geology*, *15*(9), 785–788. [https://doi.org/10.1130/0091-](https://doi.org/10.1130/0091-7613(1987)15<785:CTTGS>2.0.CO;2)  
751 [7613\(1987\)15<785:CTTGS>2.0.CO;2](https://doi.org/10.1130/0091-7613(1987)15<785:CTTGS>2.0.CO;2)

- 752 Hoffman, P. F. (1988). United Plates of America, the birth of a craton: Early Proterozoic  
753 assembly and growth of Laurentia. *Annual Review of Earth and Planetary Sciences*,  
754 *16*(1), 543–603. <https://doi.org/10.1146/annurev.earth.16.050188.002551>
- 755 Horstwood, M. S. A., Košler, J., Gehrels, G., Jackson, S. E., McLean, N. M., Paton, C., Pearson,  
756 N. J., Sircombe, K., Sylvester, P., Vermeesch, P., Bowring, J. F., Condon, D. J., &  
757 Schoene, B. (2016). Community-derived standards for LA-ICP-MS U-(Th-)Pb  
758 geochronology – Uncertainty propagation, age interpretation and data reporting.  
759 *Geostandards and Geoanalytical Research*, *40*(3), 311–332.  
760 <https://doi.org/10.1111/j.1751-908X.2016.00379.x>
- 761 Hull, J. (1988). Thickness-displacement relationships for deformation zones. *Journal of*  
762 *Structural Geology*, *10*(4), 431–435. [https://doi.org/10.1016/0191-8141\(88\)90020-X](https://doi.org/10.1016/0191-8141(88)90020-X)
- 763 Kapp, P., Manning, C. E., & Tropper, P. (2009). Phase-equilibrium constraints on titanite and  
764 rutile activities in mafic epidote amphibolites and geobarometry using titanite–rutile  
765 equilibria. *Journal of Metamorphic Geology*, *27*(7), 509–521.  
766 <https://doi.org/10.1111/j.1525-1314.2009.00836.x>
- 767 Kavanagh-Lepage, C., Gervais, F., Larson, K., Grazziani, R., & Moukhsil, A. (2022).  
768 Deformation induced decoupling between U-Pb and trace elements in titanite revealed  
769 through petrochronology and study of localized deformation. *Geoscience Frontiers*.  
770 <https://doi.org/10.1016/j.gsf.2022.101496>
- 771 Kohn, M. J. (2017). Titanite petrochronology. *Reviews in Mineralogy and Geochemistry*, *83*(1),  
772 419–441. <https://doi.org/10.2138/rmg.2017.83.13>
- 773 Kohn, M. J., & Corrie, S. L. (2011). Preserved Zr-temperatures and U–Pb ages in high-grade  
774 metamorphic titanite: Evidence for a static hot channel in the Himalayan orogen. *Earth*  
775 *and Planetary Science Letters*, *311*(1–2), 136–143.  
776 <https://doi.org/10.1016/j.epsl.2011.09.008>
- 777 Larson, K. P. (2022). ChrontouR: Geochronology plotting scripts in R [Software]. Open Science  
778 Framework. <https://doi.org/10.17605/OSF.IO/P46MB>
- 779 Lusk, A. D. J., & Platt, J. P. (2020). The deep structure and rheology of a plate boundary-scale  
780 shear zone: Constraints from an exhumed Caledonian shear zone, NW Scotland.  
781 *Lithosphere*, *2020*(1), 8824736. <https://doi.org/10.2113/2020/8824736>
- 782 Ma, S. M., Kellett, D. A., Godin, L., & Jercinovic, M. J. (2020). Localisation of the brittle  
783 Bathurst fault on pre-existing fabrics: A case for structural inheritance in the northeastern  
784 Slave craton, western Nunavut, Canada. *Canadian Journal of Earth Sciences*, *57*(6), 725–  
785 746. <https://doi.org/10.1139/cjes-2019-0100>
- 786 Mao, M., Rukhlov, A. S., Rowins, S. M., Spence, J., & Coogan, L. A. (2016). Apatite trace  
787 element compositions: A robust new tool for mineral exploration. *Economic Geology*,  
788 *111*(5), 1187–1222. <https://doi.org/10.2113/econgeo.111.5.1187>
- 789 McDonough, M. R., McNicoll, V. J., Schetselaar, E. M., & Grover, T. W. (2011).  
790 Geochronological and kinematic constraints on crustal shortening and escape in a two-  
791 sided oblique-slip collisional and magmatic orogen, Paleoproterozoic Taltson magmatic  
792 zone, northeastern Alberta. *Canadian Journal of Earth Sciences*, *37*(11), 1549–1573.  
793 <https://doi.org/10.1139/e00-089>

- 794 Miller, A. R., Cumming, G. L., & Krstic, D. (1989). U–Pb, Pb–Pb, and K–Ar isotopic study and  
795 petrography of uraniferous phosphate-bearing rocks in the Thelon Formation, Dubawnt  
796 Group, Northwest Territories, Canada. *Canadian Journal of Earth Sciences*, 26(5), 867–  
797 880. <https://doi.org/10.1139/e89-070>
- 798 Moser, A. C., Hacker, B. R., Gehrels, G. E., Seward, G. G. E., Kylander-Clark, A. R. C., &  
799 Garber, J. M. (2022). Linking titanite U–Pb dates to coupled deformation and dissolution-  
800 reprecipitation. *Contributions to Mineralogy and Petrology*, 177(3), 42.  
801 <https://doi.org/10.1007/s00410-022-01906-9>
- 802 Mulch, A., Teyssier, C., Cosca, M. A., & Vennemann, T. W. (2006). Thermomechanical analysis  
803 of strain localization in a ductile detachment zone. *Journal of Geophysical Research:*  
804 *Solid Earth*, 111(B12). <https://doi.org/10.1029/2005JB004032>
- 805 Odlum, M. L., & Stockli, D. F. (2020). Geochronologic constraints on deformation and  
806 metasomatism along an exhumed mylonitic shear zone using apatite U–Pb, geochemistry,  
807 and microtextural analysis. *Earth and Planetary Science Letters*, 538, 116177.  
808 <https://doi.org/10.1016/j.epsl.2020.116177>
- 809 Okay, A. I., Demirbağ, E., Kurt, H., Okay, N., & Kuşçu, İ. (1999). An active, deep marine strike-  
810 slip basin along the North Anatolian fault in Turkey. *Tectonics*, 18(1), 129–147.  
811 <https://doi.org/10.1029/1998TC900017>
- 812 Oriolo, S., Wemmer, K., Oyhantçabal, P., Fossen, H., Schulz, B., & Siegesmund, S. (2018).  
813 Geochronology of shear zones – A review. *Earth-Science Reviews*, 185, 665–683.  
814 <https://doi.org/10.1016/j.earscirev.2018.07.007>
- 815 Palin, R. M., & Dyck, B. (2021). Metamorphism of pelitic (Al-rich) rocks. In D. Alderton & S.  
816 A. Elias (Eds.), *Encyclopedia of Geology* (Second Edition, pp. 445–456). Academic  
817 Press. <https://doi.org/10.1016/B978-0-08-102908-4.00081-3>
- 818 Paton, C., Hellstrom, J., Paul, B., Woodhead, J., & Hergt, J. (2011). Iolite: Freeware for the  
819 visualisation and processing of mass spectrometric data. *Journal of Analytical Atomic*  
820 *Spectrometry*, 26(12), 2508. <https://doi.org/10.1039/c1ja10172b>
- 821 Phillips, R. J., Parrish, R. R., & Searle, M. P. (2004). Age constraints on ductile deformation and  
822 long-term slip rates along the Karakoram fault zone, Ladakh. *Earth and Planetary*  
823 *Science Letters*, 226(3–4), 305–319. <https://doi.org/10.1016/j.epsl.2004.07.037>
- 824 Platt, J. P., & Behr, W. M. (2011). Deep structure of lithospheric fault zones. *Geophysical*  
825 *Research Letters*, 38(24). <https://doi.org/10.1029/2011GL049719>
- 826 Powell, R., Green, E. C. R., Marillo Sialer, E., & Woodhead, J. (2020). Robust isochron  
827 calculation. *Geochronology*, 2, 325–342. <https://doi.org/10.5194/gchron-2-325-2020>
- 828 Rainbird, R. H., & Davis, W. J. (2007). U–Pb detrital zircon geochronology and provenance of  
829 the late Paleoproterozoic Dubawnt Supergroup: Linking sedimentation with tectonic  
830 reworking of the western Churchill Province, Canada. *GSA Bulletin*, 119(3–4), 314–328.  
831 <https://doi.org/10.1130/B25989.1>
- 832 Ribeiro, B. V., Lagoeiro, L., Faleiros, F. M., Hunter, N. J. R., Queiroga, G., Raveggi, M.,  
833 Cawood, P. A., Finch, M., & Campanha, G. A. C. (2020). Strain localization and fluid-  
834 assisted deformation in apatite and its influence on trace elements and U–Pb systematics.

- 835 *Earth and Planetary Science Letters*, 545, 116421.  
836 <https://doi.org/10.1016/j.epsl.2020.116421>
- 837 Scharer, K., & Streig, A. (2019). The San Andreas fault system: Complexities along a major  
838 transform fault system and relation to earthquake hazards. In *Transform Plate Boundaries*  
839 *and Fracture Zones* (pp. 249–269). Elsevier. [https://doi.org/10.1016/B978-0-12-812064-](https://doi.org/10.1016/B978-0-12-812064-4.00010-4)  
840 [4.00010-4](https://doi.org/10.1016/B978-0-12-812064-4.00010-4)
- 841 Schoene, B., & Bowring, S. A. (2006). U–Pb systematics of the McClure Mountain syenite:  
842 Thermochemical constraints on the age of the  $^{40}\text{Ar}/^{39}\text{Ar}$  standard MMhb.  
843 *Contributions to Mineralogy and Petrology*, 151(5), 615. [https://doi.org/10.1007/s00410-](https://doi.org/10.1007/s00410-006-0077-4)  
844 [006-0077-4](https://doi.org/10.1007/s00410-006-0077-4)
- 845 Scholz, C. H. (1988). The brittle-plastic transition and the depth of seismic faulting. *Geologische*  
846 *Rundschau*, 77(1), 319–328. <https://doi.org/10.1007/BF01848693>
- 847 Searle, M. P. (1996). Geological evidence against large-scale pre-Holocene offsets along the  
848 Karakoram Fault: Implications for the limited extrusion of the Tibetan plateau. *Tectonics*,  
849 15(1), 171–186. <https://doi.org/10.1029/95TC01693>
- 850 Sibson, R. H. (1977). Fault rocks and fault mechanisms. *Journal of the Geological Society*,  
851 133(3), 191–213. <https://doi.org/10.1144/gsjgs.133.3.0191>
- 852 Sibson, R. H. (1983). Continental fault structure and the shallow earthquake source. *Journal of*  
853 *the Geological Society*, 140(5), 741–767. <https://doi.org/10.1144/gsjgs.140.5.0741>
- 854 Šilerová, D., Dyck, B., Cutts, J. A., & Larson, K. (2022) GSLsz apatite and titanite  
855 geochronology [Dataset]. Open Science Framework.  
856 <https://doi.org/10.17605/OSF.IO/WP3XQ>
- 857 Spandler, C., Hammerli, J., Sha, P., Hilbert-Wolf, H., Hu, Y., Roberts, E., & Schmitz, M. (2016).  
858 MKED1: A new titanite standard for in situ analysis of Sm–Nd isotopes and U–Pb  
859 geochronology. *Chemical Geology*, 425, 110–126.  
860 <https://doi.org/10.1016/j.chemgeo.2016.01.002>
- 861 Spencer, K. J., Hacker, B. R., Kylander-Clark, A. R. C., Andersen, T. B., Cottle, J. M., Stearns,  
862 M. A., Poletti, J. E., & Seward, G. G. E. (2013). Campaign-style titanite U–Pb dating by  
863 laser-ablation ICP: Implications for crustal flow, phase transformations and titanite  
864 closure. *Chemical Geology*, 341, 84–101. <https://doi.org/10.1016/j.chemgeo.2012.11.012>
- 865 Stacey, J. S., & Kramers, J. D. (1975). Approximation of terrestrial lead isotope evolution by a  
866 two-stage model. *Earth and Planetary Science Letters*, 26(2), 207–221.  
867 [https://doi.org/10.1016/0012-821X\(75\)90088-6](https://doi.org/10.1016/0012-821X(75)90088-6)
- 868 Stearns, M. A., Hacker, B. R., Ratschbacher, L., Rutte, D., & Kylander-Clark, A. R. C. (2015).  
869 Titanite petrochronology of the Pamir gneiss domes: Implications for middle to deep  
870 crust exhumation and titanite closure to Pb and Zr diffusion. *Tectonics*, 34(4), 784–802.  
871 <https://doi.org/10.1002/2014TC003774>
- 872 Thériault, R. J. (1992). Nd isotopic evolution of the Taltson Magmatic Zone, Northwest  
873 Territories, Canada: Insights into early Proterozoic accretion along the western margin of  
874 the Churchill Province. *The Journal of Geology*, 100(4), 465–475.

- 875 Thomson, S. N., Gehrels, G. E., Ruiz, J., & Buchwaldt, R. (2012) Routine low-damage apatite  
876 U-Pb dating using laser ablation–multicollector–ICPMS. *Geochemistry, Geophysics,*  
877 *Geosystems*, 13(2), Q0AA21. <https://doi.org/10.1029/2011GC003928>
- 878 van Breemen, O., Hanmer, S., & Parrish, R. R. (1990) Archean and Proterozoic mylonites along  
879 the southeastern margin of the Slave Structural Province, Northwest Territories.  
880 *Radiogenic Age and Isotopic Studies: Report 3; Geological Survey of Canada, Paper no.*  
881 *89-2*, 55–61. <https://doi.org/10.4095/129070>
- 882 Vermeesch, P. (2018). IsoplotR: A free and open toolbox for geochronology. *Geoscience*  
883 *Frontiers*, 9(5), 1479–1493. <https://doi.org/10.1016/j.gsf.2018.04.001>
- 884 Visual DataTools, Inc. (2021). DataGraph (Version 5.0) [Software].  
885 <https://www.visualdatatools.com/>
- 886 Wallis, D., Lloyd, G. E., & Hansen, L. N. (2018). The role of strain hardening in the transition  
887 from dislocation-mediated to frictional deformation of marbles within the Karakoram  
888 Fault Zone, NW India. *Journal of Structural Geology*, 107, 25–37.  
889 <https://doi.org/10.1016/j.jsg.2017.11.008>
- 890 Walters, J. B., Cruz-Uribe, A. M., Song, W. J., Gerbi, C., & Biela, K. (2022). Strengths and  
891 limitations of in situ U–Pb titanite petrochronology in polymetamorphic rocks: An  
892 example from western Maine, USA. *Journal of Metamorphic Geology*, 40(6), 1043–  
893 1066. <https://doi.org/10.1111/jmg.12657>
- 894 Whitney, D. L., & Evans, B. W. (2010). Abbreviations for names of rock-forming minerals.  
895 *American Mineralogist*, 95, 185–187. <https://doi.org/10.2138/am.2010.3371>